

1 Diurnal cycle of the semi-direct effect from a persistent absorbing 2 aerosol layer over marine stratocumulus in large-eddy simulations

3
4 Ross J. Herbert^{1,*}, Nicolas Bellouin¹, Ellie J. Highwood¹, Adrian A. Hill²

5 ¹Department of Meteorology, University of Reading, Reading, RG6 6BB, UK

6 ²Met Office, Fitzroy Road, Exeter, EX1 3PB, UK

7 *Now at Department of Physics, University of Oxford, Oxford, OX1 3PU, UK

8 *Correspondence to:* Ross Herbert (ross.herbert@physics.ox.ac.uk)

9 The rapid adjustment, or semi-direct effect, of marine stratocumulus clouds to elevated layers of absorbing aerosols may
10 enhance or dampen the radiative effect of aerosol-radiation interactions. Here we use large eddy simulations to investigate the
11 sensitivity of stratocumulus clouds to the properties of an absorbing aerosol layer located above the inversion layer, with a
12 focus on the location, timing, and strength of the radiative heat perturbation. The sign of the daily mean semi-direct effect
13 depends on the properties and duration of the aerosol layer, the properties of the boundary layer, and the model setup. Our
14 results suggest that the daily mean semi-direct effect is more elusive than previously assessed. We find that the daily mean
15 semi-direct effect is dominated by the distance between the cloud and absorbing aerosol layer. Within the first 24 hours the
16 semi-direct effect is positive but remains under 2 Wm^{-2} unless the aerosol layer is directly above the cloud. For longer
17 durations, the daily mean semi-direct effect is consistently negative but weakens by 30 %, 60 %, and 95 % when the distance
18 between cloud and aerosol layer is 100 m, 250 m, and 500 m, respectively. Both cloud response and semi-direct effect increase
19 for thinner and denser layers of absorbing aerosol. Considerable diurnal variations in the cloud response mean that an
20 instantaneous semi-direct effect is unrepresentative of the daily mean, and that observational studies may under- or over-
21 estimate semi-direct effects depending on the observed time of day. The cloud response is particularly sensitive to the mixing
22 state of the boundary layer: well-mixed boundary layers generally result in a negative daily mean semi-direct effect, and poorly
23 mixed boundary layers result in a positive daily mean semi-direct effect. Properties of the boundary layer and model setup,
24 particularly the sea surface temperature, precipitation, and properties of the air entrained from the free troposphere, also impact
25 the magnitude of the semi-direct effect and the timescale of adjustment. These results suggest that the semi-direct effect
26 simulated by coarse-resolution models may be erroneous because the cloud response is sensitive to small-scale processes,
27 especially the sources and sinks of buoyancy.

28 1 Introduction

29 Semi-permanent decks of marine stratocumulus clouds represent an important negative radiative effect within the Earth's
30 energy budget (Hartmann et al., 1992; Hartmann and Short, 1980; Wood, 2012). In addition, the sharp inversion layer and

31 small-scale turbulent processes that characterise the formation and maintenance of these clouds represent considerable
32 uncertainty in climate models, so stratocumulus clouds remain a key uncertainty in future climate projections (Bony and
33 Dufresne, 2005; Klein et al., 2017; Wood, 2012). Marine stratocumulus clouds are sensitive to sea surface temperature (SST)
34 and large-scale atmospheric properties both above the inversion, like subsidence rate and thermodynamic properties of the
35 overlying air mass, and below the inversion, like cloud condensation nuclei sinks and sources, that impact turbulent processes
36 and dynamics throughout the boundary layer (e.g., Bretherton et al., 2013; Feingold et al., 2010; Sandu et al., 2010). Therefore,
37 small changes to these properties could result in large changes to the fluxes of radiation in the atmosphere.

38

39 Perturbations to the aerosol distribution result in a radiative forcing through both aerosol-radiation and aerosol-cloud
40 interactions; this distinction separates the radiative forcing caused by aerosol scattering and absorption of longwave and
41 shortwave radiation from that caused by the availability of cloud condensation nuclei. Aerosol-cloud interactions lead to
42 changes in cloud albedo and subsequent rapid adjustments to the cloud properties that include changes to precipitation and
43 cloud evolution (Sherwood et al., 2015). Aerosol-radiation interactions result in instantaneous changes to the extinction profile
44 (also referred to as the direct radiative effect) and therefore heating profile, which lead to rapid adjustments in the physical and
45 radiative properties of the cloud (referred to in this paper as the semi-direct effect, SDE, for convenience). Quantifying rapid
46 adjustments is important as they may act to dampen or strengthen the instantaneous forcing. Aerosol-radiation interactions
47 represent an important uncertainty in the anthropogenic radiative forcing of the climate over the industrial era, especially from
48 absorbing aerosol species such as black carbon which may result in pronounced semi-direct effects (Boucher et al., 2013). In
49 a recent climate model intercomparison study Stjern et al. (2017) found that a ten-fold increase in black carbon emissions
50 resulted in a strong positive direct effect which was partially offset by a negative SDE. Although all models agree on the sign
51 (negative) they disagree on the size of that offset, from 12 to 63 % for the models studied by Stjern et al. (2017). High-
52 resolution models that can sufficiently represent the dominant processes within the boundary layer and cloud are a powerful
53 benchmark to test the realism of the response simulated by the climate-scale models.

54

55 During the African dry season, which lasts from August to October, plumes of strongly absorbing biomass burning aerosol
56 from central Africa are transported westward over the semi-permanent marine stratocumulus deck of the Southeast Atlantic
57 Ocean, where they eventually subside and mix into the boundary layer (Das et al., 2017). Observational and modelling studies
58 suggest that elevated absorbing layers result in thicker clouds and a negative SDE (Adebisi and Zuidema, 2018; Johnson et
59 al., 2004; Wilcox, 2010), and may impact the stratocumulus-to-cumulus transition process (Yamaguchi et al., 2015; Zhou et
60 al., 2017). Once mixed into the cloud layer the absorbing aerosol exerts aerosol-radiation interactions that enhance cloud
61 evaporation (Hill and Dobbie, 2008; Johnson et al., 2004) and aerosol-cloud interactions that impact microphysical and
62 dynamical processes (e.g., Feingold et al., 2010; Gordon et al., 2018; Hill et al., 2009). Observational studies have used satellite
63 retrievals from the NASA A-Train to investigate the interaction between clouds and absorbing aerosol over the Southeast
64 Atlantic. Wilcox (2010) used co-located CALIPSO, OMI, and AMSR-E retrievals and found that for all overcast scenes liquid

65 water path (LWP) increased for high aerosol loading. This response was attributed to absorbing aerosol layers above the cloud
66 top enhancing the heating rate and decreasing entrainment across the inversion. However, satellites do not provide direct
67 observations of entrainment and an alternative explanation could be that the aerosol layers travel in relatively moist layers
68 (Adebiyi et al., 2015), increasing moisture transport across the inversion layer, even if entrainment remained unchanged. In a
69 study with a similar methodology, Costantino and Bréon (2013) separated the CALIPSO-derived aerosol layer heights into
70 cases when the smoke was close to (< 100 m) and well-separated (< 750 m) from the cloud top. The authors found that when
71 the aerosol layers are well separated from cloud top the LWP and cloud optical thickness showed no statistically significant
72 dependence on aerosol loading. These results are supported by Adebiyi and Zuidema (2018) who used satellite observations
73 and reanalysis products to show evidence that the sensitivity of low-cloud cover to elevated aerosol layers increased for small
74 cloud-aerosol gaps. These observations suggest that the distance between the elevated aerosol layer and cloud layer plays an
75 important role in the strength of the SDE. Additionally, a recent satellite study of cloud-aerosol gaps by Rajapakshe et al.
76 (2017) suggests that the elevated aerosol layers may be closer to the cloud than previously thought, which demonstrates that
77 elevated layers may have an even more important impact on the clouds.

78

79 The observations hint at the potential importance of the extent of cloud-aerosol gaps for the SDE. However, this complexity
80 is not reflected in the frameworks presented in current reviews (Bond et al., 2013; Koch and Del Genio, 2010), and there is a
81 lack of high-resolution modelling studies investigating the SDE from elevated layers of absorbing aerosol. Johnson et al.
82 (2004) used large-eddy simulation (LES) to investigate the semi-direct of absorbing aerosols on non-precipitating marine
83 stratocumulus. In an experiment where a ~ 1 km thick layer of absorbing aerosol, with an aerosol optical depth (AOD) of 0.2
84 at 550 nm, was present above the marine boundary layer throughout a 48-hr simulation, the absorbing aerosol enhanced the
85 temperature inversion at the top of the boundary layer, weakening the entrainment rate across the inversion, and producing a
86 shallower, moister boundary layer and a higher LWP. The 48-hr mean SDE was estimated to be -9.5 Wm^{-2} , almost entirely
87 cancelling a direct effect of $+10.2 \text{ Wm}^{-2}$. Yamaguchi et al. (2015) and Zhou et al. (2017) used LES models to investigate the
88 transition of marine stratocumulus to cumulus in the presence of a smoke layer. As the marine boundary layer deepened, the
89 cloud-aerosol gap decreased until the smoke layer made contact with the cloud layer. Both studies found little LWP response
90 when the smoke layer was separated by a no-aerosol gap. Yamaguchi et al. (2015) found that the elevated smoke layer reduced
91 boundary layer turbulence and cloud cover through a decrease in longwave cloud-top cooling. By isolating the aerosol heating
92 above and below the boundary layer top Zhou et al. (2017) found that when the layer was directly above the inversion layer
93 the elevated aerosol layer strengthened the inversion, inhibiting entrainment, and increased LWP and cloud cover, resulting in
94 a negative SDE. Global models have also been used to investigate the radiative impact of biomass burning aerosol in
95 stratocumulus regions (e.g., Lu et al., 2018; Penner et al., 2003; Sakaeda et al., 2011), however, Das et al. (2017) show that
96 these coarser resolution models may be unable to reproduce the observed vertical distribution of absorbing aerosol layers over
97 the southeast Atlantic, resulting in an under-representation of elevated aerosol layers and increased uncertainty in their
98 radiative impact.

100 In summary, observation and modelling studies suggest that the diurnal cycle and evolution of marine stratocumulus are
101 strongly impacted by the presence of absorbing aerosol layers at and above the top of the boundary layer. The SDE may act to
102 counteract or enhance the direct effect, resulting in either a small or large net radiative effect from aerosol–radiation
103 interactions. Yet the sensitivity of the SDE to the properties of the elevated aerosol layer has not been fully investigated. In
104 this study the UK Met Office Large Eddy Model (LEM) is used to investigate and quantify the impact that the properties of a
105 persistent elevated absorbing aerosol layer have on the cloud and radiative response of marine stratocumulus, with a focus on
106 the role that the location, timing, and strength of the heat perturbation has on the underlying cloud and boundary layer. Section
107 2 presents the LEM and its configuration and introduces a set of experiments designed to assess the SDE and its sensitivity to
108 the aerosol layer properties. Section 3 focuses on a single experiment to understand the processes that drive the cloud response
109 and SDE, then assesses the sensitivity of this response to the aerosol layer properties. Section 3 also investigates the robustness
110 of that assessment to the processes that affect the maintenance of the cloud, namely precipitation, sea surface temperature, and
111 boundary layer depth. Section 4 summarises the results, comparing to other modelling studies and observations, and discussing
112 the limitations of this study and identifying remaining questions.

113 **2 Model description and setup**

114 **2.1 Description of model**

115 The LEM (Gray et al., 2001) is a non–hydrostatic high–resolution numerical model that explicitly resolves the large–scale
116 turbulent motions responsible for the energy transport and flow. The LEM has a long track record of being used to study cloud–
117 precipitation–aerosol interactions in several cloud regimes (e.g., Efstathiou et al., 2016; Efstathiou and Beare, 2015; Hill et al.,
118 2009, 2014) and has been included in several LES intercomparison studies (e.g., Ackerman et al., 2009; van der Dussen et al.,
119 2013; Ovchinnikov et al., 2014; de Roode et al., 2016). Sub–grid scale turbulence responsible for the dissipation of kinetic
120 energy is parameterised. Prognostic variables are the three–dimensional velocity fields (u, v, w), liquid–water potential
121 temperature (θ_l), and mass–mixing ratios of water vapour (q_v), liquid water (q_l), and rain (q_r). Liquid water mass is prognosed
122 at every grid point using a condensation–evaporation scheme in which excess supersaturation is converted to liquid water and
123 vice versa for sub–saturated air. Warm rain processes are represented by a single–moment microphysics scheme that includes
124 autoconversion and cloud droplet collection following Lee (1989), sedimentation of rain, and evaporation of rain into dry air.
125 The influence of aerosol on cloud droplet number concentration is not included in this study and cloud droplet number is fixed
126 to 240 cm^{-3} for microphysical processes. Surface fluxes of moisture and heat are calculated using Monin–Obukhov similarity
127 theory (Monin and Obukhov, 1954) which predicts the surface frictional stresses and heat fluxes using the local gradients
128 between the surface and the overlying model level. For these experiments a prescribed constant sea surface temperature is
129 used. A damping layer that relaxes all prognostic variables to their horizontal mean is present above an altitude of 775 m
130 (~ 150 m above the cloud layer; see Sect. 2.2) with a height scale of 650 m and a timescale of 30 s. This prevents the reflection

131 of gravity waves at the rigid top boundary and prevents the production of trapped buoyancy waves above the inversion layer
132 (Ackerman et al., 2009). The subsidence rate w_s is represented by a height dependent function $w_s(z) = -Dz$ for which large-
133 scale divergence (D) is prescribed. The model is run with a variable time step with a maximum of 0.5 seconds. The LEM
134 radiation scheme, described by Edwards and Slingo (1996), is a two-stream solver with six shortwave spectral bands and eight
135 longwave bands that calculates the vertical distribution of radiative fluxes and heating rates. The scheme includes six aerosol
136 species with wavelength and humidity-dependent mass absorption coefficients, mass scattering coefficients, and asymmetry
137 factors. A single value for the mean cloud droplet effective radius of $10\ \mu\text{m}$ is prescribed in the radiation scheme.

138 2.2 Model setup

139 All simulations are three dimensional with periodic lateral boundary conditions. The model domain is 5200 m in the horizontal
140 with a horizontal grid resolution of 40 m, and 2600 m in the vertical with a variable vertical grid resolution with ~ 6 m resolution
141 at the cloud top and inversion and less than 10 m throughout the boundary layer (BL). The LEM is configured here to produce
142 a stratocumulus with a consistent diurnal cycle over an 8-day timescale. The initial profiles of θ_1 and q_1 were taken from
143 Johnson et al. (2004) and based on subtropical marine stratocumulus observations from the First International Satellite Cloud
144 Climatology Project Regional Experiment (FIRE) (Hignett, 1991) in the subtropical Pacific Ocean. A series of 10-day
145 simulations without absorbing aerosol were run with varying subsidence rates to obtain steady-state profiles of θ_1 and q_1 that
146 would produce a consistent stratocumulus layer with a maximum cloud top height of 600 m. The resulting initialisation profiles
147 are shown in Table 1; the BL is $0.6\ \text{g kg}^{-1}$ drier than in Johnson et al. (2004) and Hill et al. (2008) due to the inclusion of
148 precipitation in our study and a cooler SST, which was necessary in order to attain a similar cloud LWP to these studies. The
149 large-scale divergence D is set to $5.5 \times 10^{-6}\ \text{s}^{-1}$, giving a subsidence rate of $w_s = -3.3\ \text{mm s}^{-1}$ at the cloud top. D and w_s are
150 within the observed range for marine stratocumulus regions (Zhang et al., 2009) and of similar magnitude to other
151 stratocumulus LES studies (e.g., Johnson et al., 2004; De Roode et al., 2014). The initial profiles describe a well-mixed moist
152 BL capped by a sharp (10 K) inversion at 600 m with a warm and dry free troposphere (FT) above the inversion. To account
153 for a source of large-scale heat divergence a cooling rate of $0.1\ \text{K day}^{-1}$ is applied. This value is lower than the $1.0\ \text{K day}^{-1}$
154 used by Johnson et al. (2004) and Hill et al. (2008) because the greater cooling rates result in an unstable cloud top height in
155 our simulations which is undesirable as we require a consistent cloud layer to isolate the cloud response due to the absorbing
156 aerosol. A prescribed surface pressure of 1012.5 hPa is used, and zonal and meridional geostrophic winds are $6.0\ \text{m s}^{-1}$ and -
157 $1.0\ \text{m s}^{-1}$, respectively. The radiation scheme is set up for consistency with the FIRE campaign with a time-varying solar zenith
158 angle for mid-July at the co-ordinates 33°N , 123°W . Radiation calculations are performed for all grid points within the domain
159 every 30 seconds. Surface roughness is fixed at $2 \times 10^{-4}\ \text{m}$ and SST at 287.2 K.

160

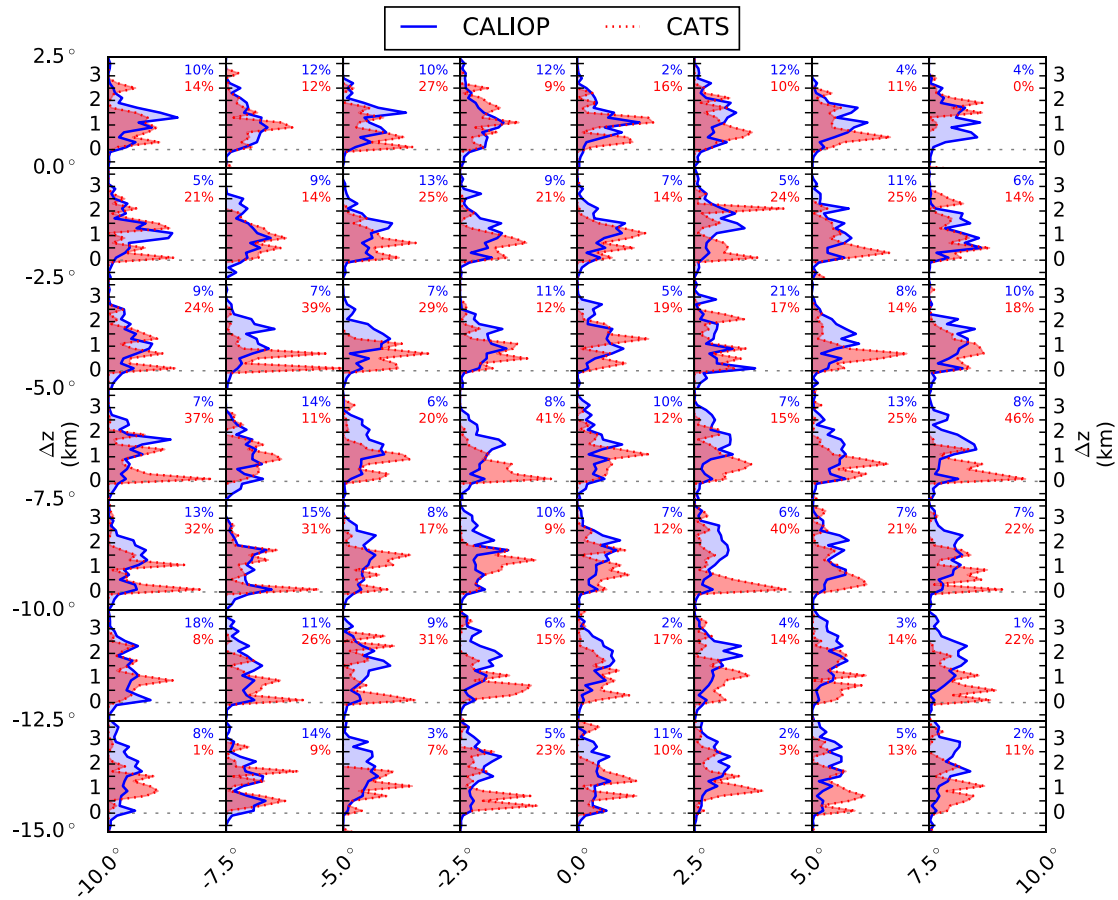
161 **Table 1. Initial profiles used in the control simulations**

Altitude (m)	Liquid–water potential temperature (K)	Total water mixing ratio (g kg ⁻¹)
0	287.5	9.0
600	287.5	9.0
601	297.0	5.5
750	300.0	5.5
1000	301.7	5.5
1500	303.2	5.5
2600	304.0	5.5

162

163 **2.3 Setup of elevated–aerosol experiments**

164 To simulate the effect of an elevated absorbing–aerosol layer above the cloud top, a layer of dry aerosol is prescribed,
165 consisting of soot–like and water–soluble–like aerosol, representing predominantly absorbing and scattering species,
166 respectively. The interaction of longwave and shortwave radiation with the aerosol layer results in localised heating rates that
167 are coupled to the LEM. The prescribed aerosol layer properties include the height of layer base above the inversion layer
168 (referred to as the cloud–aerosol gap), geometric thickness, mean single–scattering albedo (SSA), and AOD. These properties
169 are set at the beginning of the experiment and applied during each call to the radiation scheme. Using the prescribed geometric
170 thickness of the aerosol layer, a balance between the mass–mixing–ratio of soot and water–soluble aerosol is used to achieve
171 the desired SSA and AOD throughout the simulation (see Appendix for more details on the method employed). In these
172 experiments SSA is 0.9, which is towards the higher end of the range of SSA for biomass burning aerosol (Peers et al., 2016)
173 and thus represents a relatively conservative value for the absorption of the aerosol layer.



174

175 **Figure 1. Normalised frequency of occurrence of gap distance between cloud layer top and aerosol base heights from CALIOP (blue**
 176 **solid line) and CATS (red dotted line) for single layer coincidences of aerosol and cloud in the months of July, August, and September**
 177 **(2007–2016 for CALIOP; 2015–2017 for CATS) over the southeast Atlantic (15°S to 2.5°N, 10°W to 10°E). Layer heights are binned**
 178 **from -1.5 to 5.5 km in 200 m increments and data in each grid has been normalised to the maximum frequency across the whole**
 179 **study area. The percentage of scenes where the aerosol layer base is less than 360 m above the cloud top height is shown in the top**
 180 **right of each subplot for each dataset.**

181

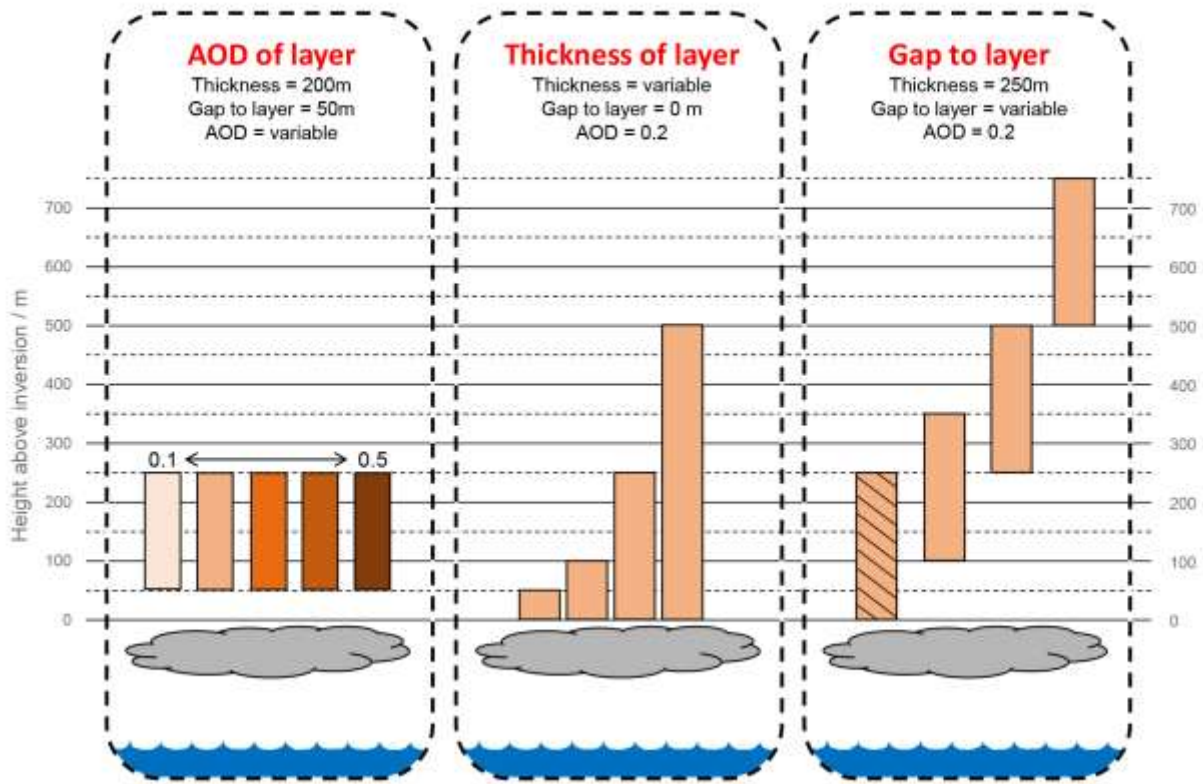
182 Realistic cloud–aerosol gaps are needed for the elevated–aerosol experiments. They are taken from observations from the
 183 CALIPSO Cloud–Aerosol Lidar with Orthogonal Polarization (CALIOP) instrument (5–km resolution, 532 nm Aerosol Layer
 184 Product and Cloud Layer Product, v4.10, level 2 data) and the NASA Cloud–Aerosol Transport System
 185 (CATS) lidar (5 km resolution, V3–00, Mode 7.2, Level 2 Daytime Operational Layer Data Product, 1064 nm wavelength)
 186 over the Southeast Atlantic Ocean (15°S to 2.5°N, 10°W to 10°E). The distance Δz between the retrieved cloud top and the
 187 aerosol base heights is determined from scenes where vertical profiles only include a single layer of low cloud (cloud top
 188 below 2.5 km) and a single layer of aerosol. Figure 1 shows the normalised frequency of occurrence of Δz in 2.5-degree grids

189 for all scenes within July, August, and September between 2007 and 2016 for CALIOP data and between 2015 and 2017 for
190 CATS data. Both datasets display considerable variation in Δz at all locations, yet the CATS dataset has a higher percentage
191 of scenes in close proximity (within 360 m) of the cloud top compared to CALIOP. This agrees well with the study of
192 Rajapakshe et al. (2017) who found that the 532 nm wavelength used in the CALIOP retrieval often over-estimates the distance
193 between cloud top and aerosol base, whereas the longer 1064 nm wavelength used by CATS provides a more reliable estimate.
194 The CALIOP and CATS analysis (Figure 1) suggests that elevated aerosol layers predominantly exist within 1500 m of the
195 cloud top with a common occurrence of layers in close proximity (less than 360 m) to the cloud. In-line with this we focus on
196 layers of absorbing aerosol that range from directly above the cloud layer ($\Delta z = 0$ m) to elevated layers at $\Delta z = 500$ m, and we
197 additionally examine the role of the aerosol layer depth which, for a given AOD, will impact the vertical distribution and
198 strength of the localised heat perturbation.

199

200 A schematic of the experiments designed to investigate the sensitivity of the SDE and cloud diurnal cycle to key layer
201 properties, namely the AOD, geometric thickness, and the cloud-aerosol gap, is shown in Figure 2. The first set investigates
202 the sensitivity of the SDE to the strength of the aerosol layer absorption. Following AOD observations by Chand et al. (2009),
203 the AOD of the layer is varied from 0.1 to 0.5 while keeping the geometric thickness constant at 200 m and the cloud-aerosol
204 gap at 50 m. The second set of experiments investigates the sensitivity of the cloud response to the geometric thickness of the
205 aerosol layer at constant AOD. This type of experiment aims to understand the importance of correctly retrieving the full
206 geometric extent of the aerosol layer (altitudes of the layer top and base) from a satellite retrieval when the AOD is known;
207 variables often provided in combined satellite products such as CCCM (Kato et al., 2010, 2011). This is a known deficiency
208 with retrievals made using wavelengths that are strongly attenuated by biomass burning aerosol such as the 532 nm channel
209 currently used in the CALIOP aerosol products (Rajapakshe et al., 2017). For these experiments the geometric thickness of the
210 aerosol layer is increased from 50 to 500 m with no cloud-aerosol gap and are effectively experiments with variable density
211 of aerosol particles, since with a fixed AOD the aerosol layer mass-mixing ratio decreases with increasing geometric thickness
212 of the layer. The final set of experiments investigates the impact of the cloud-aerosol gap by placing the aerosol layer base
213 from 0 to 500 m above the inversion layer while keeping geometric thickness and AOD constant. A full list of experiments
214 performed is presented in Table 2. We use one of the experiments, referred to as the base experiment, to provide an initial in-
215 depth analysis of the cloud and radiative response. In the base experiment (hatched experiment in Figure 2) a 250 m thick
216 absorbing aerosol layer with an AOD of 0.2 is placed directly above the inversion layer.

217



218

219 **Figure 2. Schematic showing the experiments performed for the aerosol-sensitivity simulations. The hatched experiment is named**
 220 **the base experiment and is used to provide initial analysis of the semi-direct effect in Sect. 3.2. AOD stands for aerosol optical depth**
 221 **and is given at a mid-band wavelength of 505 nm.**

222

223 The SDE is calculated following Johnson et al. (2004) as a residual of the difference in top-of-atmosphere net radiation (F_{TOA})
 224 between the aerosol and no-aerosol simulations, minus the direct radiative effect (DRE):

225

$$\text{SDE} = F_{\text{TOA,aerosol}} - F_{\text{TOA,no-aerosol}} - \text{DRE} \quad (1)$$

226

227 where F_{TOA} is calculated using the upward (\uparrow) and downward (\downarrow) fluxes of longwave (LW) and shortwave (SW) radiation:

228

$$F_{\text{TOA}} = F_{\text{TOA,SW}}^{\downarrow} - (F_{\text{TOA,SW}}^{\uparrow} + F_{\text{TOA,LW}}^{\uparrow}) \quad (2)$$

229

230 DRE is calculated as the difference between F_{TOA} and that obtained in a second, diagnostic, call to the radiation scheme with
 231 the same profiles of liquid water, water vapour, and atmospheric gases, but without aerosol. This second call is only performed
 232 for the simulations with aerosol present.

234 **Table 2. Breakdown of all experiments performed. AOD stands for aerosol optical depth and is given at a mid-band wavelength of**
 235 **505 nm.**

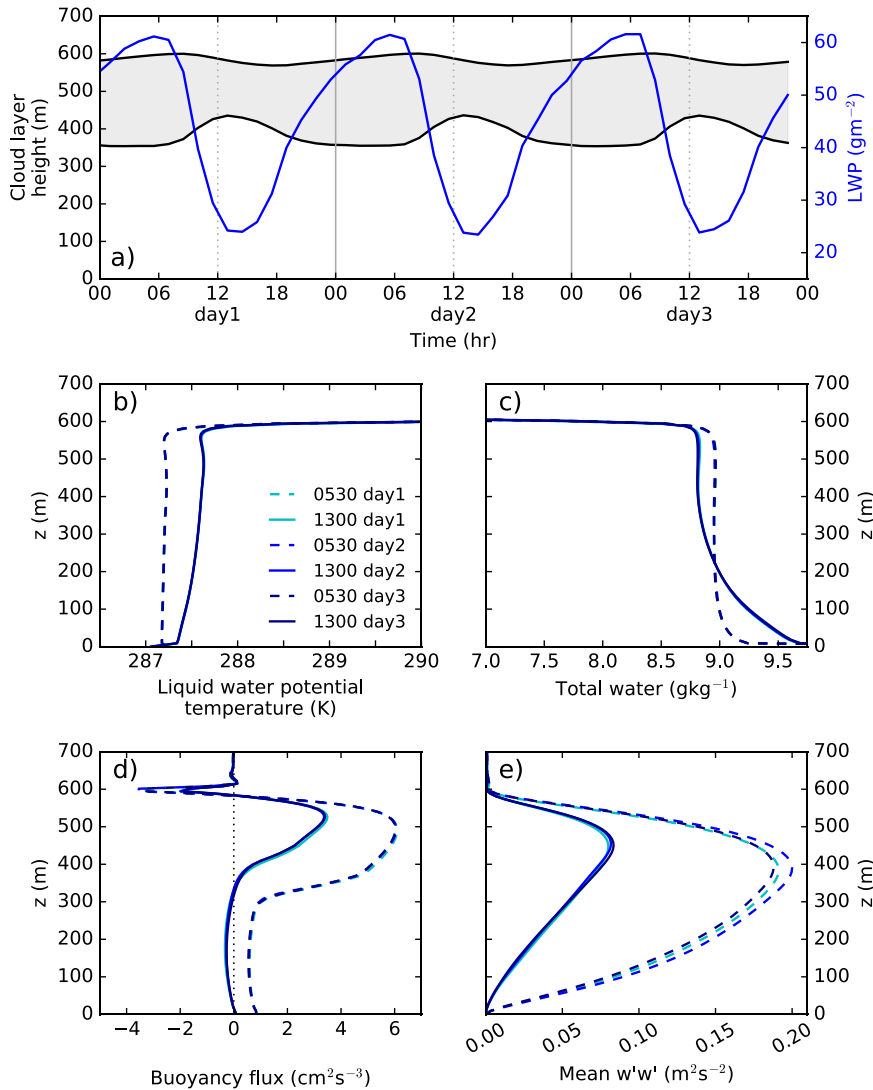
Type of experiment	Layer properties		
	Cloud–aerosol gap (m)	Layer thickness (m)	Layer AOD
Variable AOD	50	200	0.1
	50	200	0.2
	50	200	0.3
	50	200	0.4
	50	200	0.5
Variable thickness	0	50	0.2
	0	100	0.2
	0	250	0.2
	0	500	0.2
Variable gap	0*	250	0.2
	100	250	0.2
	250	250	0.2
	500	250	0.2

* Base experiment used for initial analysis

236 **3 Results**

237 **3.1 No–aerosol experiment**

238 The no–aerosol experiment is initialised then run for fifteen days without the presence of an aerosol layer. The first five days
 239 are used as a spin–up period that allows the BL to reach a steady state; the following three days (days 6, 7, and 8 of the
 240 simulation) are shown in Figure 3.



242

243 **Figure 3. Evolution of domain averaged cloud properties in the no-aerosol simulation including: a) cloud top and base (black lines;**
 244 **left axis), and liquid water path (blue line; right axis); and vertical profiles taken at 0530 (dashed lines) and 1300 (solid lines) on each**
 245 **day for b) liquid water potential temperature, c) total water mass mixing ratio, d) buoyancy flux, and e) the variance in vertical**
 246 **velocity $w'w'$.**

247 The no-aerosol experiment produces a cloud-topped BL with strong diurnal variations. During the daytime, cloud top height
 248 decreases and cloud base height increases, thinning the cloud and producing a diurnal cycle of LWP that reaches a maximum
 249 of 60 g m^{-2} at dawn and a minimum of 25 g m^{-2} just after midday (Figure 3a). The precipitation rate at the surface (not shown)
 250 ranges from a maximum of 0.2 mm day^{-1} at night to a minimum of 0.01 mm day^{-1} during the day. For a cloud with a LWP of
 251 60 g m^{-2} this is within the range of observations presented by Abel et al. (2010). The diurnal cycle of the cloud layer can be
 252 separated into a growth phase between 1400 and 0600, and a decay phase between 0700 and 1300. The growth phase is driven

253 by pronounced buoyancy production during the night (Figure 3d) from longwave cloud–top cooling and evaporative cooling
254 of entrained air, which drives strong turbulent motion throughout the BL (Figure 3e). During the daytime, solar heating reduces
255 the buoyancy flux (Fig. 3d) through an offset in the longwave cooling and reduces turbulence throughout the BL (Fig. 3e).
256 This weakens the BL circulation and prevents mixing throughout the BL and promotes a decoupled state in which the flux of
257 moisture from the surface to the cloud is insufficient to maintain the cloud base height, as evident from the non–constant BL
258 profiles of θ_l (Figure 3b) and q_l (Figure 3c) at 1300 hours. The weakened flux and solar heating of the cloud drives the lifting
259 condensation level upwards and causes the cloud base to increase with height, producing the decay phase. During the daytime
260 weakened BL eddies are unable to ‘push’ against the subsidence at the BL top, which decreases the BL depth and cloud top
261 height. Due to the different processes that control the cloud top and cloud base diurnal variations, the cloud top height minimum
262 occurs about 2 hours after the cloud base reaches its maximum. The cloud layer, LWP and thermodynamic profiles in Figure
263 3 (a – e) show very little change over the three days of the simulation and present a stratocumulus deck with a consistent
264 diurnal cycle in a steady state. This provides a suitable simulation to use as control for the elevated–aerosol experiments.

265 **3.2 Cloud response to elevated aerosol layer in the base experiment**

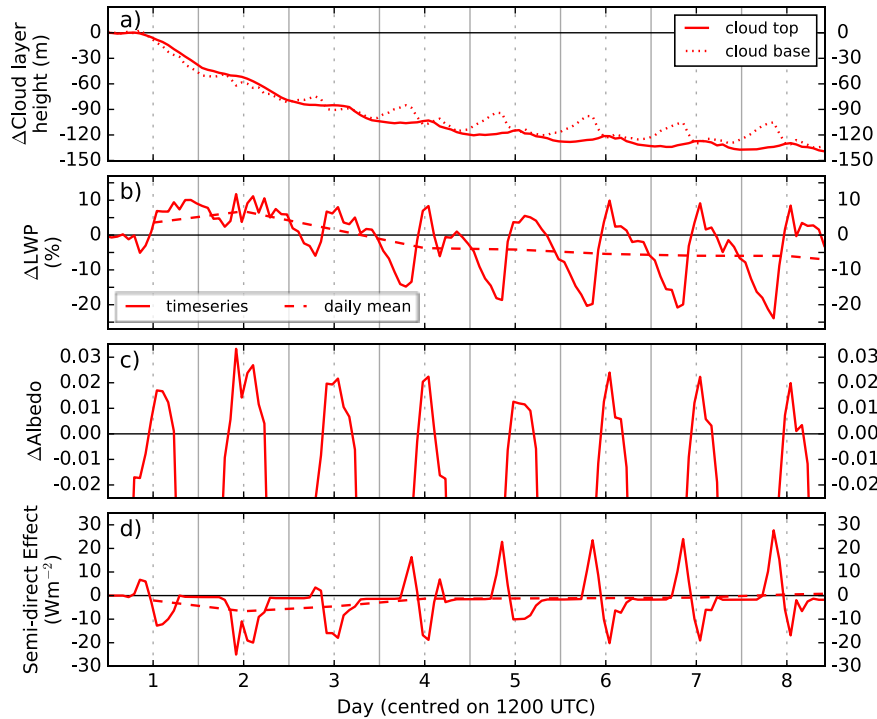
266 We begin with the base experiment (hatched experiment in Figure 2) where a 250 m thick absorbing aerosol layer with an
267 AOD of 0.2 is placed directly above the inversion layer. Following a five–day spin–up period without aerosol, the simulation
268 runs for a further ten days with the aerosol layer present. The domain–averaged cloud response following the introduction of
269 aerosol is shown in Figure 4 and compared to the no–aerosol simulation.

270

271 The simulations show that the absorbing aerosol drives changes in the diurnal cycle of cloud depth and LWP, predominantly
272 through changes in the cloud base height. The presence of the absorbing aerosol drives a decrease in cloud top height (Figure
273 4a) which occurs predominantly in the afternoon and evening and is indicative of a decrease in entrainment across the inversion
274 layer. During the initial two days the cloud base (Figure 4a) decreases in altitude ~ 10 m more than the cloud top resulting in a
275 thicker cloud, however from day three onwards there is less growth of the cloud throughout the evening and early morning,
276 followed by less thinning throughout the day. Compared to the cloud in the presence of no aerosol, the introduction of the
277 absorbing aerosol layer results in relatively less LWP (Figure 4b) during the growth phase of the cloud and more LWP during
278 the decay phase.

279

280 The SDE (Figure 4d) has a strong diurnal cycle that is directly driven by modifications to the cloud albedo diurnal cycle (Figure
281 4c) and shows considerable sensitivity to the LWP response during the cloud decay phase around midday. In the first three
282 days the albedo response is positive from mid–morning to the late afternoon. This drives an overall negative daily mean SDE.
283 The length of time with a positive albedo response gets shorter as the simulation progresses, driving an increasingly positive
284 SDE in the morning that cancels out, on a daily mean, the negative SDE in the afternoon. Consequently, the daily mean SDE
285 is negative for the initial three days but almost net zero SDE from the fourth day onwards.



287

288 **Figure 4. 10-day timeseries of domain-averaged cloud response to a layer of aerosol directly above the boundary layer inversion**
 289 **with an aerosol optical depth of 0.2 and geometric thickness of 250 m. Plots show the difference between the no-aerosol simulation**
 290 **and the simulation with an elevated aerosol layer for a) cloud top height (solid line) and cloud base height (dotted line), b) cloud**
 291 **liquid water path (LWP), c) albedo, and d) the semi-direct effect. Solid lines in b), c), and d) show the timeseries of the response and**
 292 **dashed lines in b) and d) show the daily mean.**

293

294 The cloud response and SDE are therefore markedly different in the initial phase compared to the steady-state that is reached
 295 after 6 or 7 days following the introduction of the absorbing aerosol layer. In that steady-state phase the BL depth has decreased
 296 by ~ 130 m ($\sim 20\%$) and the diurnal cycle response in cloud thickness has stabilised. This suggests there are timescales in the
 297 response to the introduction of the aerosol layer: a short-term response that can be interpreted as a rapid adjustment of the
 298 humidity profile, and longer-term response that can be interpreted as a new equilibrium state for the BL sources of moisture,
 299 turbulence, and heat.

300

301 This study focuses on the initial response because it is more relevant for real-world understanding as the aerosol perturbation
 302 is unlikely to remain constant for several days, and the lifetime of stratocumulus decks is generally on the order of a few days
 303 only. However, the steady-state response provides insight into the key drivers behind the BL modifications.

304 3.2.1 Initial response in the base experiment

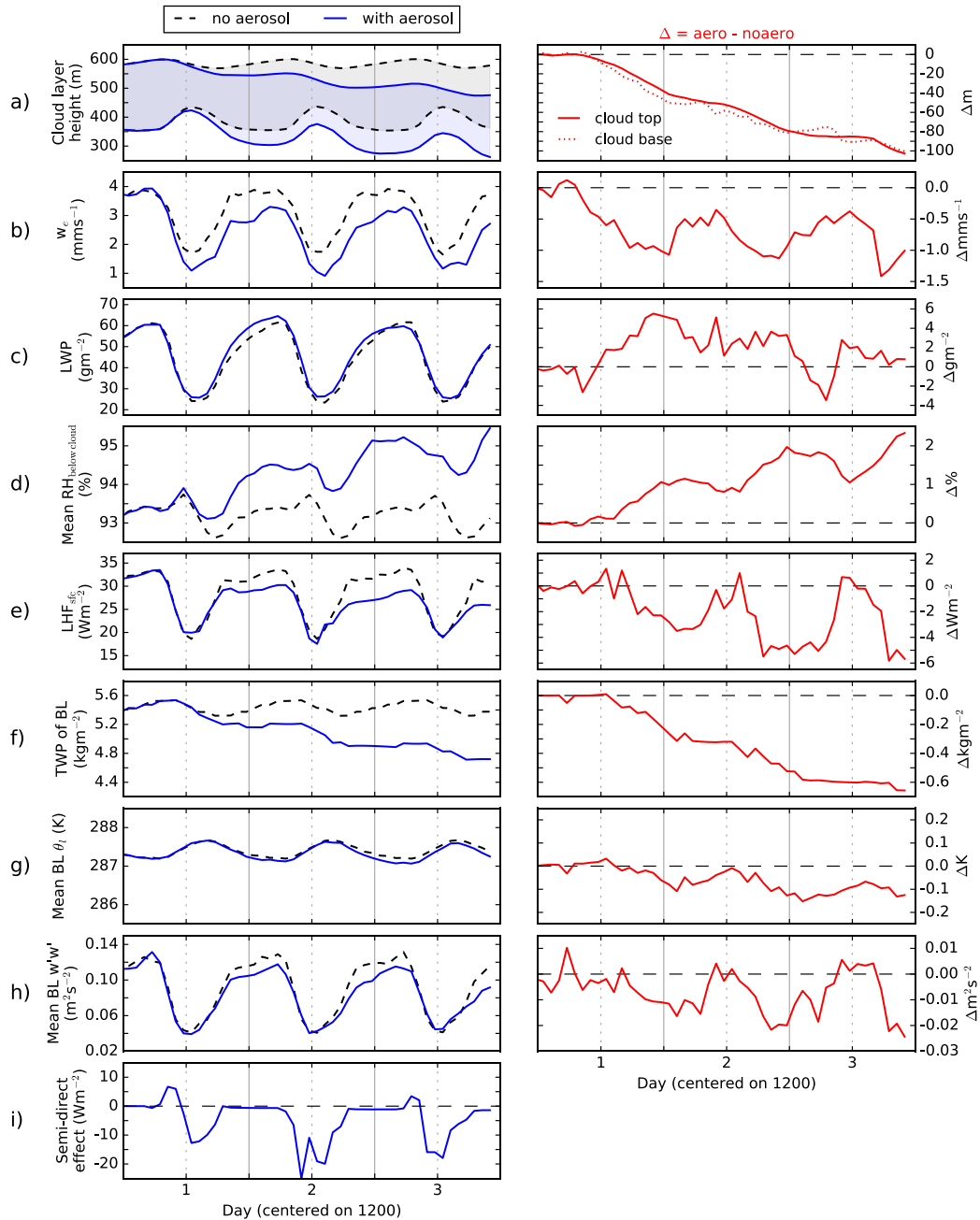
305 The domain-averaged timeseries of the response in the first three days following the introduction of the aerosol layer (days 6,
306 7, and 8 of the simulation) are shown in Figure 5. The initial response of the cloud to the elevated aerosol layer is driven by
307 the weakening of the entrainment rate ($w_e = \frac{dz_{\text{cloudtop}}}{dt} - w_s$) and subsequent increase in the mean RH below cloud which acts
308 to produce a thicker cloud in the first two days. Solar radiation heats the elevated absorbing aerosol layer above the inversion
309 layer. Strengthening of the temperature inversion at the top of the BL drives a weakened w_e (Figure 5b) which causes the BL
310 depth to decrease (Figure 5a). Simultaneously, there is an increase in mean RH below cloud (Figure 5d), which allows the
311 cloud base height to decrease (Figure 5a) and the LWP to increase (Figure 5c); this response continues for the first two days,
312 after which the LWP starts to display a diurnal response with a decrease in LWP during the night and an increase in the
313 afternoon. The increase in RH occurs due to the weakened w_e which reduces the amount of warm dry FT air that is mixed into
314 the BL and allows the sub-cloud layer to maintain a higher RH. The relatively small decrease in potential temperature of ~ 0.1
315 K (Fig. 5g) suggests that the RH response is driven by an increase in available water vapour. There is little response of the
316 cloud before sunrise, which suggests a weak insulating effect of the aerosol layer on longwave fluxes at the cloud top. This is
317 supported by a lack of systematically weakened cloud-top longwave cooling (Fig. S1 in the supplementary information), which
318 would be expected for an increased downwelling longwave flux from the aerosol layer.

319

320 The thinner cloud (lower LWP; Fig. 5a) on the morning of the third day is driven by changes to the supply of moisture to the
321 cloud layer. The enhanced RH below cloud and weakened vertical motions (Figure 5h) drive a strong reduction in surface
322 evaporation as demonstrated by the decrease in latent heat flux (LHF; Figure 5e), especially during the night. By the end of
323 day three the LHF at the surface has reduced by 20% and the total water path (TWP) of the BL (Figure 5f) has reduced by
324 10%. During the night when the BL is well mixed this reduction in TWP prevents the cloud from developing to the same extent
325 as in the no-aerosol simulation, resulting in a thinner cloud when the sun rises. This process is amplified by the reduced BL
326 dynamics which will weaken the flux of moisture from the sub-cloud region to the cloud.

327

328 The thicker cloud (enhanced LWP; Fig. 5a) on the afternoon of the third day is driven by relatively stronger coupling with the
329 surface moisture fluxes at midday, which produces a slightly thicker cloud and a negative SDE (Figure 5i). Under no-aerosol
330 conditions, shortwave absorption by the cloud stabilises the cloud layer during the day, which results in a degree of decoupling
331 between the surface layer and cloud base (Figure 3). When an elevated absorbing aerosol layer is present, the decrease in cloud
332 layer height, following the BL depth decrease, allows better coupling to the surface (see Fig. S2 in the supplementary
333 information), which becomes increasingly important around midday when BL dynamics are weakest (Figure 5h). The
334 enhanced source of moisture to cloud base, along with weakened entrainment of dry FT air, prevents the cloud from thinning
335 to the same extent. Although the change in LWP is only $2\text{--}3 \text{ g m}^{-2}$, this amounts to a 10% increase, which helps drive a strong
336 negative SDE at midday and early afternoon.



337

338 **Figure 5.** 3-day timeseries showing the initial domain averaged cloud response to a layer of absorbing aerosol in the base
 339 experiment (0 m cloud–aerosol gap, 250 m thick layer, and AOD of 0.2). In the first column the black dashed lines refer to the
 340 control experiment (no–aerosol) and solid blue lines to the experiments with the aerosol layer present. The second column shows
 341 the cloud response (red solid line). The plots show a) the altitude of the cloud base and top, b) the entrainment rate w_e , c) the liquid
 342 water path (LWP), d) the mean relative humidity (RH) between the ocean surface and the cloud base, e) the latent heat flux (LHF)
 343 from the surface, f) the total water path (TWP) of the boundary layer (BL), g) mean liquid–water potential temperature (θ) of the
 344 BL, h) the mean BL vertical velocity variance ($w'w'$), and i) the semi–direct effect.

345

346 The analysis of the initial cloud response shows that the first two days are characterised by a general thickening of the cloud
347 driven by the reduction in w_e across the temperature inversion and subsequent enhanced RH profile below cloud via an increase
348 in water vapour. The weakened w_e , BL dynamics, and moisture flux from the surface begin to dry the BL resulting in less
349 cloud growth overnight, whilst the lower cloud base enhances coupling to the surface moisture fluxes during the middle of the
350 day, and less cloud decay.

351

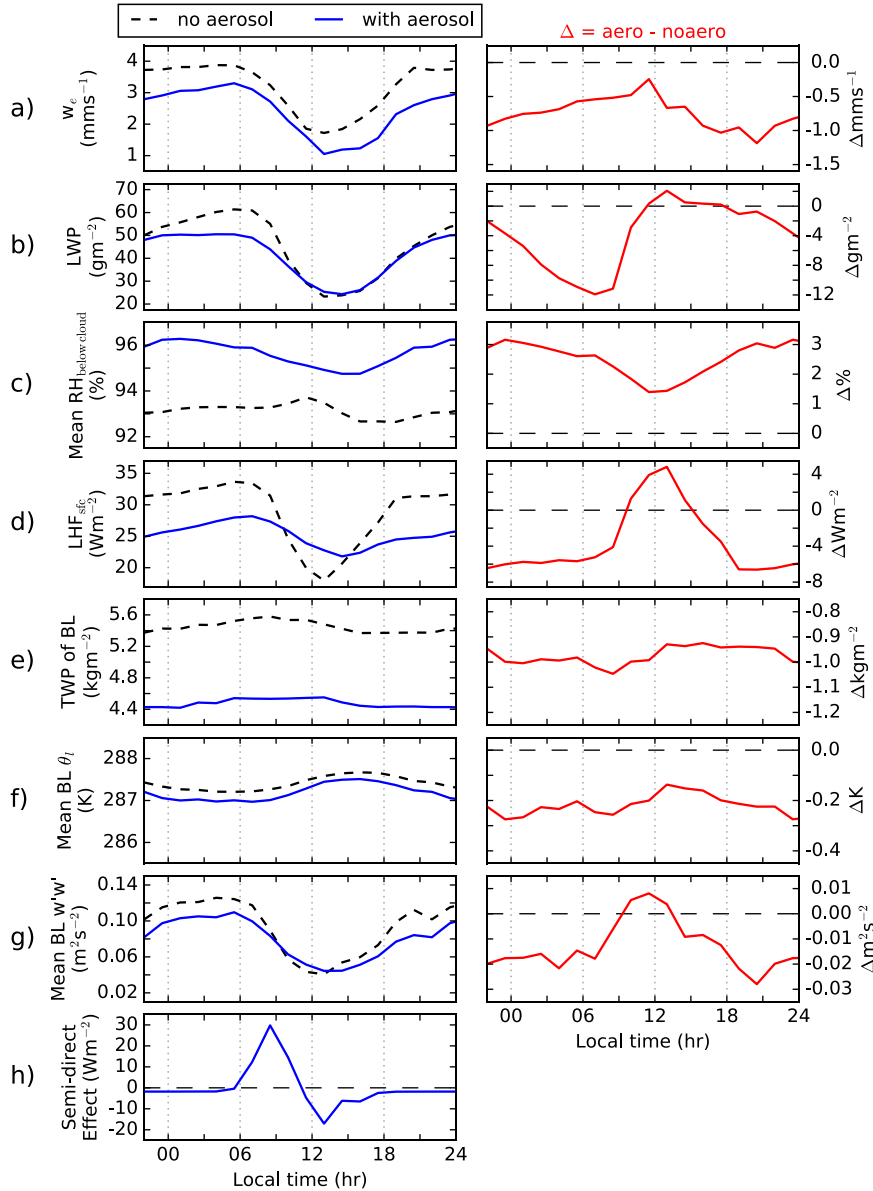
352 3.2.2 Steady-state response in the base experiment

353 The final three days of the 15-day base experiment provide a mean diurnal cycle of the cloud response. Although aerosol
354 layers do not persist above stratocumulus decks for so long in reality, the steady-state response provides insight into the key
355 drivers behind the BL modifications. The steady-state response of the cloud to the elevated aerosol layer, shown in Figure 6,
356 shows strong similarities to the third day of the initial response: the growth phase of the cloud (Figure 6b) is weakened,
357 producing a thinner cloud in the morning, and the decay phase of the cloud (Figure 6b) is weakened, producing a thicker cloud
358 in the early afternoon. This modification to the diurnal cycle of the cloud is driven by an increased coupling between surface
359 moisture flux and cloud base during the daytime (see Fig. S2 in the supplementary information) and an overall decrease in
360 TWP of the BL and weakened dynamics overnight. The decrease in cloud layer height allows better mixing beneath the cloud
361 base, which enhances the evaporation of moisture from the surface between 0900 and 1500 (Figure 6d); this is evident from
362 the weekend diurnal cycle in mean RH below cloud (Figure 6c), which usually occurs due to poor mixing, and the strengthened
363 BL dynamics at midday (Figure 6g). The small response in mean BL potential temperature of -0.2 K (Fig. 6f) strengthens the
364 hypothesis that the RH response below cloud is driven by changes in available water vapour, rather than the decrease in
365 temperature, although it is worth noting that this decrease in temperature will act to slightly increase the RH.

366

367 The weakened cloud growth phase overnight occurs due to a 15% reduction in TWP of the BL (Figure 6e) and a reduction in
368 mean BL vertical motions overnight of ~20%, indicated by the mean BL vertical velocity variance ($w'w'$) in Figure 6g. The
369 reduction in w_e (Figure 6a) and subsequent changes to below-cloud water vapour set up a positive feedback mechanism with
370 BL dynamics: vertical motions in the BL are considerably weakened throughout the night and slightly strengthened at midday.
371 Although there is a decrease in LWP there is no systematic impact to the cloud-top longwave cooling due to its weak sensitivity
372 to LWP above 50 g m^{-2} (van der Dussen et al., 2013; Garrett and Zhao, 2006). The weakened BL circulation is therefore due
373 to a reduction in entrainment. The mixing of dry air into the cloud layer results in evaporation and a cooling which generates
374 buoyancy; a reduction in entrainment therefore weakens cloud-top buoyancy production. These combined changes result in
375 reduced vertical motions within the BL, which reduce surface evaporation, cloud LWP, and buoyancy production from
376 condensation at cloud base, which allow the reduced vertical motions to persist. A partial offset to this process occurs during
377 midday when stronger coupling to the surface results in enhanced transport of water vapour to the cloud base.

378 The steady-state response establishes itself by the third day of the simulation. The daily mean steady-state SDE (Figure 6h)
 379 results from a balance between the degree to which the BL TWP has decreased, producing a positive SDE in the morning, and
 380 the degree to which the midday coupling is enhanced, producing a negative SDE in the afternoon. In both cases modifications
 381 to BL depth, and thus w_e , play a significant role in cloud response and SDE.
 382



383

384 **Figure 6. Domain averaged cloud response to a layer of absorbing aerosol directly above the inversion in the base experiment (0 m**
 385 **cloud-aerosol gap, 250-m thick layer, and AOD of 0.2) for the mean diurnal cycle using the final three days of the 15-day simulation.**
 386 **In the first column the black dashed lines refer to the control experiment (no-aerosol) and solid blue lines to the experiments with**

387 the aerosol layer present. The second column shows the cloud response (red solid line). The plots show a) the entrainment rate w_e ,
388 b) the liquid water path (LWP), c) the mean relative humidity (RH) between ocean surface and cloud base, d) the latent heat flux
389 (LHF) from the surface, e) the total water path (TWP) of the boundary layer (BL), f) mean liquid–water potential temperature (θ_l)
390 of the BL, g) the mean BL vertical velocity variance ($w'w'$), and h) the semi–direct effect.

391 3.3 Sensitivity of initial response to aerosol layer properties

392 Figure 7 shows timeseries for the aerosol layer–sensitivity experiments. In this analysis the inversion strength $\Delta\theta_l$ is determined
393 between altitudes z_{upper} and z_{lower} . The value of z_{upper} is the topmost altitude where the absolute gradient $\left|\frac{d\theta_l}{dz}\right|$ is 25% of its
394 maximum, and z_{lower} is the lowermost altitude where $\left|\frac{d\theta_l}{dz}\right|$ is 2.5% of its maximum. The upper threshold is determined at a
395 higher percentage of $\left|\frac{d\theta_l}{dz}\right|$ than the lower threshold to limit spurious values occurring from aerosol layers close to the inversion
396 layer that impact θ_l .

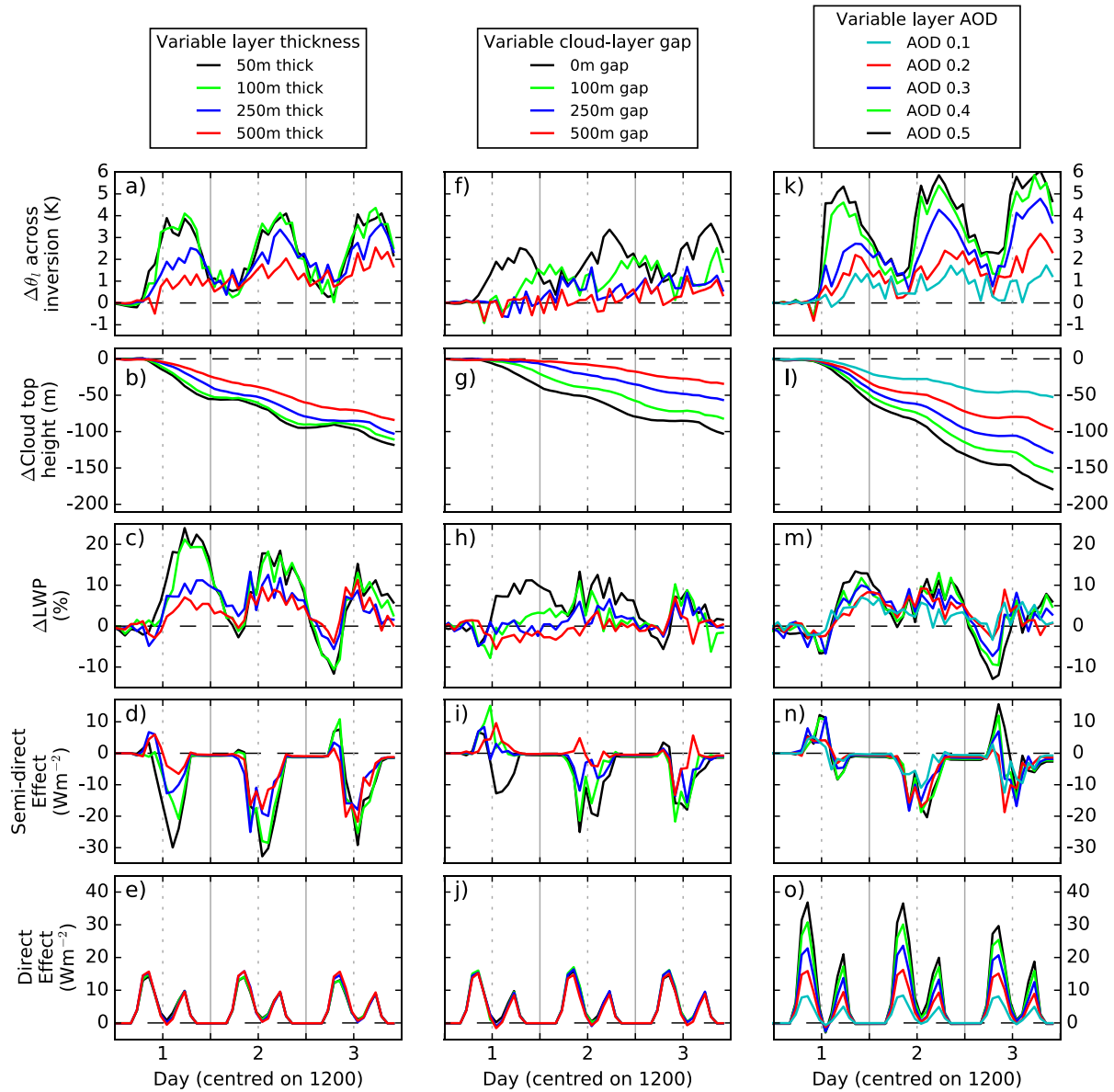
397 3.3.1 Cloud response

398 The majority of experiments show a positive spike in SDE (Figure 7d, i and n) just before midday on the first day. This occurs
399 due to the lag–time in response between the direct impact to the cloud from changes to w_e , and the increase in sub–cloud RH.
400 Figure S1 in the supplementary information focuses on the response in the initial 24 hours. The positive SDE is driven by the
401 decrease in LWP caused by an increase in cloud base height (Fig. 5a and Fig. S1a) without a corresponding change in cloud
402 top height. The decrease in w_e weakens buoyancy production throughout the cloud layer (Fig. S1c), which drives a reduced
403 moisture flux within the cloud and to the cloud base (Fig. S1d). As the day progresses the continued reduction of w_e results in
404 an increase in mean below–cloud RH and a recovery, or increase, of the LWP. This explains why stronger perturbations to the
405 entrainment rate on the first day (such as when the layer is close to the cloud) results in a quicker recovery of the LWP (Fig.
406 7c, h, and m). This result suggests the specific timing of the incoming aerosol plume may play a role in the cloud response and
407 SDE on the first day.

408

409 Geometrically thinner aerosol layers equate, for a given AOD, to a greater aerosol mass mixing ratio and therefore stronger
410 heating. This results in a stronger inversion layer (Figure 7a) and stronger modification to the LWP response (Figure 7c) and
411 SDE (Figure 7d), especially on the first day. This produces a stronger inversion layer, weaker w_e , and a decrease in BL depth
412 (Figure 7b). For the two thinnest layers the cloud top height decreases at a faster rate during the day than at night, which
413 correlates with the peak heat perturbation. For thicker layers the heat perturbation extends further into the night; this
414 corresponds with the delay in time for the heating towards the top of the layer to reach the inversion layer and drives a steadier
415 reduction in BL depth when compared to the thinner layers. By the third day the BL has started to adjust and less dependence
416 on aerosol layer thickness is apparent, however the thinner layers cause the BL to dry out at a quicker rate, thus producing a
417 stronger positive SDE on the morning of the third day.

418



420

421 **Figure 7.** 3-day timeseries showing the sensitivity of the initial cloud response (difference between the no-aerosol simulation and the
 422 simulation with an elevated aerosol layer) to the properties of the elevated absorbing aerosol layer. The three columns correspond
 423 to experiments where systematic changes have been made to the aerosol layer thickness (a – e), cloud-aerosol gap (f – j), and aerosol
 424 layer AOD (k – o).

425

426 Increasing the cloud-aerosol gap leads to a weaker and increasingly delayed cloud top height (Figure 7g) and LWP response
 427 (Figure 7h) driven by changes in peak strengthening of the inversion (Figure 7f); this is most pronounced in the first two days.

428 Only aerosol layers directly above the inversion trigger a considerable cloud response on the first day because of the relatively
429 rapid strengthening of the inversion layer and weakening of w_e which forces the cloud top downwards more rapidly than the
430 RH profile can adjust, resulting in a deeper cloud base. On the second day a cloud response is seen with gaps up to 100 m and
431 by the third day all gaps lead to a response in cloud LWP. The delay in response is driven by the delay in the inversion layer
432 strengthening. In the free troposphere the advection of the heat perturbation is driven by subsidence, therefore, greater cloud–
433 aerosol gaps require more time for the heat perturbation to reach the cloud top. Simultaneously longwave cooling acts to
434 weaken the heat perturbation throughout its advection, which drives a relatively weaker strengthening of the temperature
435 inversion as the cloud–aerosol gap increases.

436
437 The initial cloud top response (Figure 7l) displays a strong dependence on the AOD of the aerosol layer throughout the three
438 days with greater AOD resulting in a greater response. As with geometric layer thickness, larger AODs absorb more radiation
439 and drive a stronger heat perturbation and inversion strength (Figure 7k). So larger AODs result in a thicker cloud and a more
440 negative SDE. On the third day layers with the largest AODs, which have had the greatest impact on cloud top height and w_e ,
441 exhibit a considerably thinner cloud, driving an increasingly positive SDE in the morning.

442
443 In summary, the layer–sensitivity experiments show that on the first day the initial response is for the cloud top to drop quicker
444 than the cloud base, resulting in a thinner cloud and a positive SDE in the morning, the magnitude of which is primarily driven
445 by the proximity of the aerosol layer with the cloud top. With no gap between the inversion at cloud top and aerosol layer, the
446 afternoon of the first day is characterised by a thicker cloud and negative SDE which increases in magnitude for stronger heat
447 perturbations. The second day is generally characterised by an increase in the LWP at midday which drives a negative SDE
448 and is dependent on the location and properties of the aerosol layer. By the third day a consistent pattern occurs: the cloud is
449 consistently thinner in the morning and thicker at midday, the magnitude of which is dependent on the strength of the
450 perturbation.

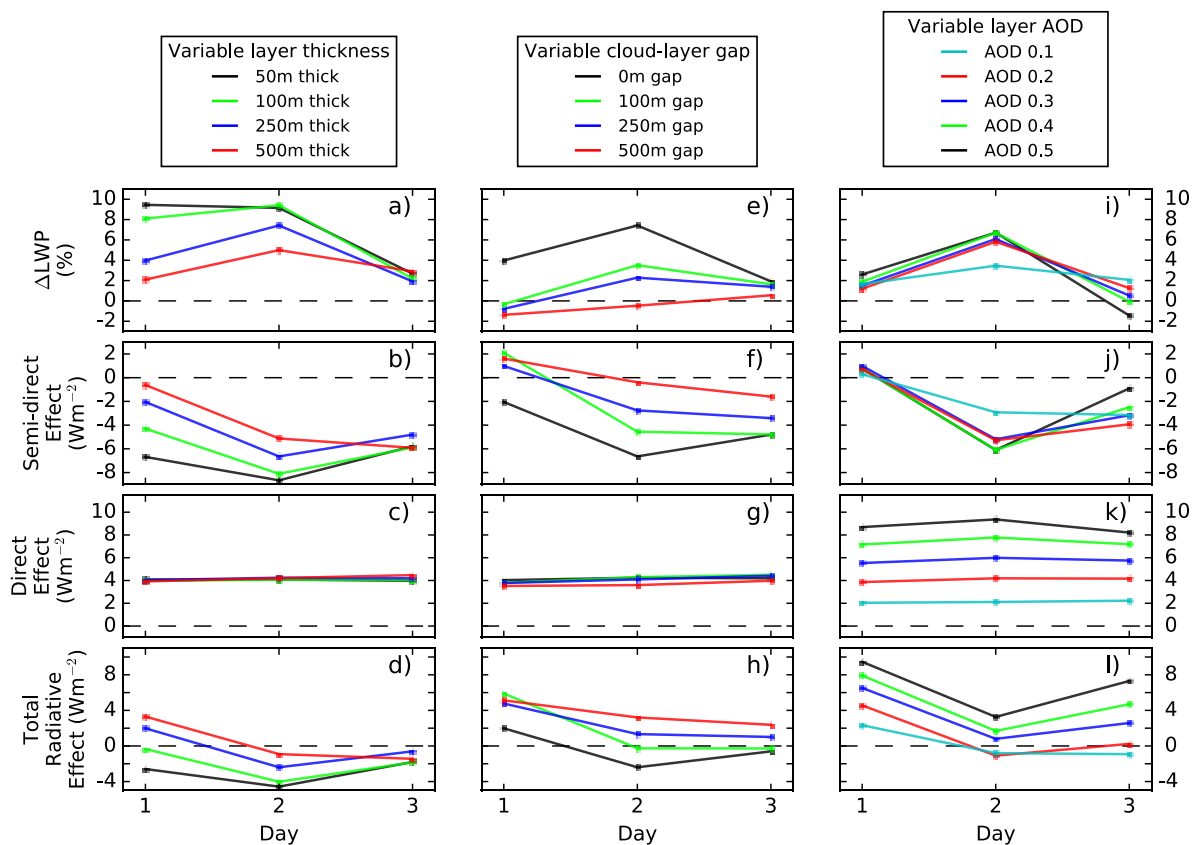
451 3.3.2 Radiative response

452 Figure 8 shows timeseries of the daily mean radiative effects for the layer–sensitivity experiments. The immediate radiative
453 response following the introduction of the absorbing aerosol layer is primarily dependent on the distance between the inversion
454 layer and aerosol layer base. When there is no cloud–aerosol gap the increase in LWP results in a negative SDE; thinner layers
455 and larger AODs increase the inversion layer strengthening and drive a stronger negative SDE on the first day. When any
456 cloud–aerosol gap is present there is little LWP response on the first day due to the delayed inversion layer strengthening,
457 however, all experiments with a gap present are characterised by a small positive SDE. For the experiments with a 50 m gap
458 (variable AOD experiments) the delay is short enough that there is an increase in LWP in the evening of the first day (Figure
459 8i).

460

461 On the second and third day the SDE is negative for all experiments; the magnitude of the SDE increases for thinner layers,
 462 closer to the inversion layer. When a cloud–aerosol gap is present the AOD tends to have little impact on the magnitude of the
 463 SDE. The rate at which the BL moisture content decreases, itself a factor of how strongly w_e is perturbed, results in variations
 464 in which day the peak SDE occurs. In experiments with gaps smaller than 100 m the maximum SDE is reached on the second
 465 day, whereas for gaps larger than or equal to 100 m the maximum occurs on the third day. In all experiments the third day is
 466 characterised by a decrease in the daily mean LWP response which is primarily driven by less cloud growth overnight and in
 467 the morning (see Figure 7c, h and m) and becomes more pronounced as the temperature inversion strengthens. The thinner
 468 cloud in the morning helps to shift the daily mean SDE towards zero.

469



470

471 **Figure 8. Daily mean radiative impact to the elevated aerosol layer properties over the initial three days following the introduction**
 472 **of the aerosol layer for systematic changes to a) – d) aerosol layer thickness, e) – h) cloud–aerosol gap, and i) – l) aerosol optical**
 473 **depth of layer.**

474

475 The properties of the aerosol layer have a considerable impact on the total radiative effect, calculated as the sum of the DRE
 476 and SDE (Figure 8d, h, and l). Generally, the SDE acts to counteract the positive DRE and in some cases results in an overall
 477 negative total radiative effect. In all experiments the total radiative effect is sensitive to the layer properties, whereas DRE is

478 only sensitive to the layer AOD. In many instances the SDE is greater in magnitude than the DRE, with the second day
 479 constituting the period of time with the greatest impact. The relative insensitivity of the SDE to changes in AOD suggest that
 480 layers with a moderate AOD (~ 0.2) may have the strongest overall radiative impact due to the relatively low DRE; however,
 481 the behaviour may change for increasing gaps.

482

483 The results of the experiments are summarised in Table 3 with the daily mean SDE alongside the means for the periods before
 484 and after midday. The daily mean SDE is only consistently negative throughout the three days when there is no cloud–aerosol
 485 gap. This result is consistent with Johnson et al. (2004) who similarly found a negative SDE for a ~ 1000 m layer of absorbing
 486 aerosol (AOD of 0.2, SSA of 0.88) directly above the inversion layer. Johnson et al. (2004) calculated a mean SDE of -9.5 Wm^{-2}
 487 and a mean DRE of 10 Wm^{-2} . These magnitudes are greater than in this study but similarly show the SDE is of approximately
 488 equal magnitude to the DRE and of opposite signs. Our results also show that geometrically thin, but optically thick, aerosol
 489 layers will have a stronger forcing than a thicker layer with the same AOD due to a stronger localised heat perturbation; this
 490 effect is most prominent on the first day. When a gap to the aerosol layer base is present, as is predominantly observed (Fig.
 491 1), our results show that the short–term SDE is likely to be weakly positive but then becomes negative once the BL has been
 492 mixed, which usually occurs during the first night when BL mixing occurs, highlighting a sensitivity to the specific arrival
 493 timing of the incoming plume. On the second and third day the magnitude of the SDE then depends on the AOD, cloud–aerosol
 494 gap, and aerosol layer thickness.

495

496 **Table 3. Mean semi–direct effect (in Wm^{-2}) for each of the aerosol experiments shown in Figure 2 and Table 2. Mean values are**
 497 **presented for each day (Daily), between 0000 and 1200 hours (am), and between 1200 and 2400 (pm).**

Type of experiment				<i>Day 1</i>			<i>Day 2</i>			<i>Day 3</i>		
	gap	dz	AOD	Daily	am	pm	Daily	am	pm	Daily	am	pm
Variable gap	0	250	0.2	-2	1	-5	-7	-6	-7	-5	-4	-6
	100	250	0.2	2	4	0.4	-5	-5	-4	-5	-5	-5
	250	250	0.2	1	2	0.3	-3	-3	-3	-3	-3	-4
	500	250	0.2	2	1	2	-0.4	1	-1	-2	-3	-0.5
Variable thickness	0	50	0.2	-7	-2	-12	-9	-5	-13	-6	-2	-10
	0	100	0.2	-4	-1	-8	-8	-5	-11	-6	-2	-10
	0	250	0.2	-2	1	-5	-7	-6	-7	-5	-4	-6
	0	500	0.2	-1	2	-3	-5	-4	-6	-6	-5	-7
Variable AOD	50	200	0.1	0.3	2	-1	-3	-3	-3	-3	-2	-4
	50	200	0.2	1	2	-0.1	-5	-5	-6	-4	-4	-4
	50	200	0.3	1	2	-0.1	-5	-5	-5	-3	-1	-5
	50	200	0.4	1	2	-1	-6	-4	-8	-2	-0.4	-5

498

499 Table 3 highlights the diurnal variations in the SDE. The SDE is generally more negative after midday but that contrast varies
500 with aerosol layer properties. Geometrically thin, optically thick layers, directly above the inversion layer display the strongest
501 contrast with the daily mean SDE dominated by the mean after midday. When a gap is present there is less contrast and both
502 time periods are generally representative of the daily mean, until the BL begins to dry out significantly in the high AOD
503 experiments. These results demonstrate that there are often strong diurnal variations in the SDE which are sensitive to the
504 aerosol layer properties and suggest that observations of the SDE made within a small window of time, e.g., those from polar
505 orbiting satellites, may be unrepresentative of the daily mean SDE.

506 3.4 Sensitivity to boundary layer and cloud properties

507 This section investigates the robustness of the results and conclusions from Sect. 3.3. The parameter space considered in this
508 section includes previous LEM studies, such as Hill and Dobbie (2008) and Johnson et al. (2004), and the range of
509 environmental forcings observed within marine stratocumulus regions.

510

511 The first set of sensitivities focus on the model setup and includes no precipitation from the cloud (*noRain*) and an enhanced
512 large-scale advective heat tendency of -0.5 Kday^{-1} (*05cool*).

- 513 • In the *noRain* setup the production of precipitation is switched off. Stratocumulus frequently produce precipitation in
514 the form of drizzle (Leon et al., 2009) yet studies often simplify simulations by focusing on non-precipitating
515 stratocumulus (e.g., Hill and Dobbie, 2008; Johnson et al., 2004). Precipitation redistributes moisture from the cloud
516 layer to the sub-cloud layer, promoting BL stability and acting to reduce BL dynamics and cloud LWP (Ackerman
517 et al., 2009).
- 518 • In the *05cool* sensitivity, the magnitude of the large-scale advective heat tendency is increased from -0.1
519 to -0.5 Kday^{-1} . That parameter accounts for the equatorward transport of the large-scale air mass and is negative in
520 subtropical marine regions. This value can be estimated using large-scale reanalyses (e.g., Johnson et al., 2004) or
521 used as a balancing term to prevent subsidence heating (e.g., Duynkerke et al., 2004) and represents a degree of
522 variability in LES setups.

523

524 The second set of sensitivities focuses on properties of the BL that may impact the diurnal cycle and maintenance of the cloud.

- 525 • In the *SST-1K* and *SST+1K* setups, SST is decreased and increased by 1K, respectively, while keeping the BL depth
526 at 600 m. Stratocumulus decks in the Atlantic and Pacific Oceans are observed over a wide range of sea surface
527 temperatures (Sandu and Stevens, 2011; Wood, 2012). As the SST increases the differential temperature across the
528 surface-air boundary increases, resulting in more pronounced surface moisture and sensible heat fluxes.

- 529 • The *wetFT* setup increases the mass mixing ratio of water vapour in the FT by $+0.4 \text{ g kg}^{-1}$ to assess the impact of the
530 water vapour content of the entrained air on the SDE. Trajectory analyses from the Pacific and Atlantic Oceans by
531 Sandu et al. (2010) show that the mass mixing ratio of water vapour in the FT varies spatially and temporally, ranging
532 from 1.0 to 7.5 g kg^{-1} at 700 hPa ; this result is supported by in-situ data summarised by Albrecht et al. (1995).
- 533 • The *800-m* and *1000-m* setups increase the height of the temperature inversion by 200 and 400 m , respectively, by
534 changing the large-scale divergence rate and initial profiles of θ_l and q_t , while keeping SST constant at 287.2 K .
535 Observations show that cloud top heights in regions of semi-permanent stratocumulus coverage (southeast Atlantic,
536 southeast Pacific, and northeast Pacific) typically range from ~ 500 to $\sim 1500 \text{ m}$ (Muhlbauer et al., 2014; Painemal et
537 al., 2014; Wyant et al., 2010) with variations driven by SST and subsidence.

538
539 To isolate the cloud response due to the aerosol layer, the cloud-sensitivity experiments are initialised using profiles that
540 produce an approximately constant stratocumulus cloud layer at the top of the BL following the method described in Sect. 2.2.
541 Table 4 shows the resulting initial profiles and large-scale divergence rates for each setup. The same set of experiments from
542 Sect. 3.3 are performed for each setup, along with a simulation without aerosol to calculate the BL response to the aerosol
543 perturbation. The daily mean SDE on day 2 following the introduction of the absorbing aerosol layer (day 7 of the simulation)
544 is shown in Table 5 for each setup and aerosol experiment. For the *control* setup the SDE values are the same as shown in
545 Figure 8.

546

547 **Table 4. Initial profiles of liquid-water potential temperature (θ_l in K) and total liquid mass-mixing ratio (q_t in g kg^{-1}) against**
548 **altitude (z in m) for each cloud-sensitivity setup. Values in parentheses indicate the large-scale divergence rate (D in s^{-1}) used for**
549 **each setup. All setups result in a stable stratocumulus cloud deck at the top of the boundary layer.**

	<i>noRain</i> (5.4×10^{-6})		<i>05cool</i> (6.2×10^{-6})		<i>SST-1K</i> (4.75×10^{-6})		<i>SST+1K</i> (5.75×10^{-6})		<i>wetFT</i> (5.25×10^{-6})		<i>800m</i> (4.0×10^{-6})			<i>1000m</i> (2.75×10^{-6})		
z	θ_l	q_t	θ_l	q_t	θ_l	q_t	θ_l	q_t	θ_l	q_t	z	θ_l	q_t	z	θ_l	q_t
0	287.5	9.0	287.3	9.0	286.5	8.6	288.3	9.4	287.3	9.0	0	287.3	9.0	0	287.3	9.0
600	287.5	9.0	287.3	9.0	286.5	8.6	288.3	9.4	287.3	9.0	800	287.3	9.0	1000	287.3	9.0
601	297.0	5.5	296.0	5.5	296.0	5.5	297.2	5.5	297.0	5.9	801	297.0	5.9	1001	297.0	5.9
750	300.0	5.5	299.0	5.5	300.0	5.5	300.0	5.5	299.5	5.9	900	299.5	5.9	1100	299.5	5.9
1000	301.7	5.5	300.3	5.5	301.7	5.5	301.7	5.5	301.5	5.9	1200	301.5	5.9	1300	301.5	5.9
1500	303.2	5.5	301.5	5.5	303.2	5.5	303.2	5.5	302.6	5.9	1700	302.6	5.9	1900	302.6	5.9
2600	304.0	5.5	302.8	5.5	304.0	5.5	304.0	5.5	303.8	5.9	2600	303.8	5.9	2600	303.8	5.9

550

551 3.4.1 Sensitivity to model setup

552 Comparing the no-aerosol simulations, the removal of precipitation results in stronger BL dynamics and a greater peak in
553 LWP (+15 g m⁻²) than the *control* setup. The *noRain* setup is characterised by a consistent increase in the magnitude of the
554 SDE by 1 Wm⁻² when a cloud-aerosol gap is present and up to 3 Wm⁻² when there is no gap. In the *control* setup the presence
555 of the aerosol layer increases cloud LWP, which is partially offset by an increase in precipitation. In the *noRain* setup that
556 partial offset is not allowed, resulting in relatively enhanced LWP response and SDE.

557

558 When compared to the *control* setup, increasing the cooling rate of the large-scale advective heat tendency results in stronger
559 BL dynamics, enhanced cloud-top entrainment of warm dry air, and enhanced surface LHF (which acts as a feedback to
560 enhanced entrainment). As the processes maintaining the cloud layer become more important, they become more sensitive to
561 perturbations. Therefore, when the aerosol layer is present in the *05cool* setup, the responses of w_e , LHF, and below-cloud
562 moisture flux are stronger than in the *control* setup and the simulations are characterised by a quicker decrease in the TWP of
563 the BL. However, this only becomes prominent on the third day and results in little difference from the *control* setup over the
564 first two days.

565 3.4.2 Sensitivity to BL properties

566 In the no-aerosol simulations warmer SST drives an enhanced below-cloud moisture flux but a lower LWP due to an increase
567 in BL temperature. The warmer BL also leads to stronger in-cloud buoyancy production. When the aerosol layer is present the
568 LWP response increases with SST, driving a stronger negative SDE in all experiments. The cloud response is particularly
569 sensitive to SST when the aerosol layer is near the cloud top. As discussed in Sect. 3.2, the initial response from the weakened
570 w_e , and subsequently enhanced RH, occurs quicker than the moisture source from the surface can readjust to. The reduction in
571 w_e and BL depth are equivalent for all SST, but the greater flux of moisture from warmer SST results in a greater increase in
572 mean q_t and RH perturbation, leading to a lower cloud base, thicker cloud, and tending to push the SDE towards a more
573 negative daily mean. The sensitivity of the radiative response is driven both by the SST and the perturbation to w_e , therefore
574 stronger heat perturbations closer to the cloud top result in a more pronounced sensitivity to SST.

575

576 The no-aerosol simulation for the *wetFT* setup is characterised by an LWP +5 g m⁻² greater than the *control* setup, with slightly
577 weaker surface evaporation. This increase in LWP is caused by entrainment of slightly moister FT air in the *wetFT* setup,
578 allowing the BL to maintain a greater mean RH. The mixing of entrained air has a smaller impact on the cloud humidity, which
579 then does not need to be balanced as strongly from a source at the surface. When the aerosol layer is present the weakened w_e
580 therefore has a smaller impact on the RH response of the BL, which results in a smaller SDE. This setup shows that the degree
581 by which the entrained air impacts the cloud plays an important role in the strength of the SDE: very dry FT air will play a
582 more important role in reducing RH, so that a perturbation to w_e will have a greater impact on the cloud response.

583 **Table 5. Daily mean semi-direct radiative effect for the second day following the introduction of the absorbing aerosol layer for**
584 **control and cloud-sensitivity setups. All values are in daily mean Wm^{-2} . Layer properties include the cloud-aerosol gap ('gap', in**
585 **metres), the geometric thickness of the layer ('dz', in metres), and the aerosol optical depth (AOD) of the layer given at a mid-band**
586 **wavelength of 505 nm.**

Type of experiment	gap	dz	AOD	<i>control</i>	<i>noRain</i>	<i>05cool</i>	<i>SST-1K</i>	<i>SST+1K</i>	<i>wetFT</i>	<i>800-m</i>	<i>1000-m</i>
Variable gap	0	250	0.2	-7	-8	-5	-5	-8	-6	4	17
	100	250	0.2	-5	-6	-5	-3	-7	-3	6	10
	250	250	0.2	-3	-4	-4	-1	-5	-2	6	6
	500	250	0.2	0	-1	-2	1	0	0	4	2
Variable thickness	0	50	0.2	-9	-12	-7	-7	-13	-8	0	18
	0	100	0.2	-8	-10	-7	-5	-11	-7	2	20
	0	250	0.2	-7	-8	-5	-5	-8	-6	4	17
	0	500	0.2	-5	-7	-5	-2	-8	-5	5	11
Variable AOD	50	200	0.1	-3	-5	-3	-1	-3	-3	6	7
	50	200	0.2	-5	-7	-4	-3	-6	-5	5	15
	50	200	0.3	-5	-9	-4	-4	-8	-6	5	22
	50	200	0.4	-6	-9	-5	-4	-10	-5	6	25
	50	200	0.5	-6	-7	-5	-4	-10	-5	5	26

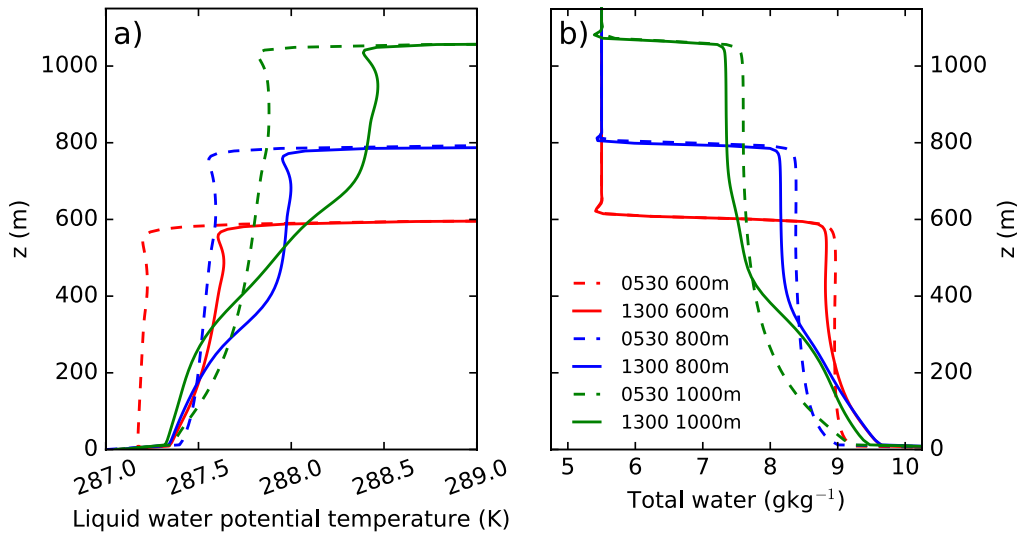
587

588 3.4.3 Sensitivity to BL depth

589 As the BL depth increases its temperature increases and the TWP of the BL decreases. Figure 9 shows the profiles of θ_1 and q_1
590 for the three setups (*control*, *800-m*, *1000-m*) during the time of strongest (0530 hours) and weakest (1300 hours) BL dynamics.
591 During the period with weakest dynamics the degree of coupling, or mixing, between the sub-cloud and cloud layers is
592 weakened. This reduces the flux of water vapour from the surface layer to the cloud, resulting in an accumulation of water
593 vapour close to the surface (Figure 9b). That redistribution becomes more pronounced as the BL depth increases, increasing
594 BL decoupling.

595

596 Increasing the BL depth has a dramatic effect on the sign and magnitude of the SDE shown in Table 5. The SDE switches sign
597 from negative for a 600-m deep BL in the *control* setup to positive in the *800-m* and *1000-m* setups. The SDE in the *800-m*
598 setup is roughly of equal magnitude to the *control* but the *1000-m* setup is considerably greater in magnitude, peaking at
599 $+26 \text{ Wm}^{-2}$. Responses for the base experiment shown in Figure 10 help to understand why the BL depth has such a strong
600 impact on the SDE. In all setups the cloud top height decreases by ~ 100 m over the three days (Figure 10a, g, and m), driven
601 by similar changes in w_e (Figure 10e, k, and q), however the response in cloud base height depends on the simulation and
602 accounts for the variation in LWP response (Figure 10b, h, and n). In the *1000-m* setup (Figure 10m) the cloud base decreases
603 less than the cloud top throughout the timeseries, driving a consistently reduced LWP.

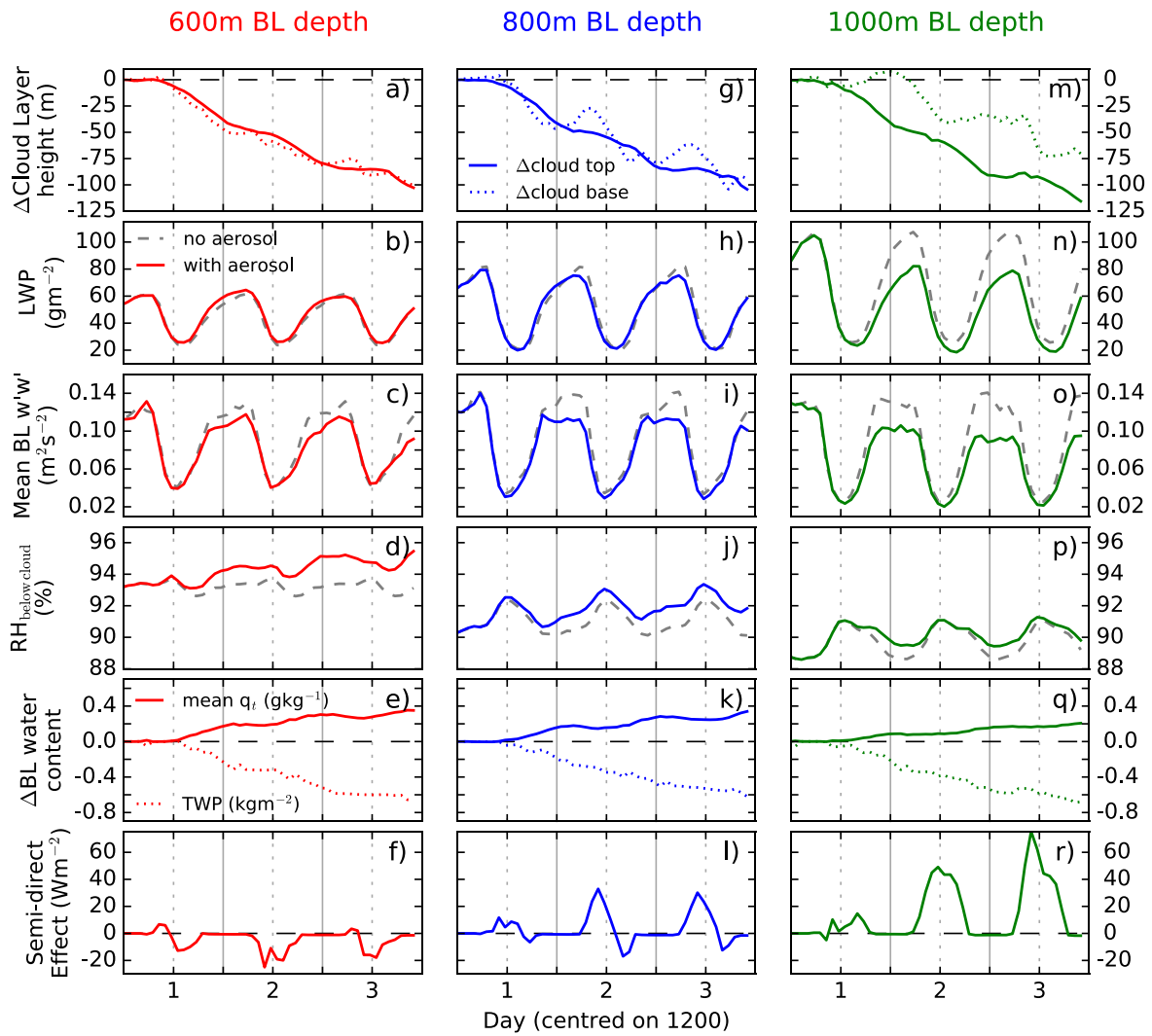


605

606 **Figure 9. Vertical profiles of a) liquid water potential temperature and b) total water mass mixing ratio taken at 0530 (dashed lines)**
 607 **and 1300 (solid lines) on day 1 (after spin-up) for the no-aerosol simulations.**

608

609 As shown in Figure 9 the degree of decoupling between the sub-cloud and cloud layers increases with BL depth. The diurnal
 610 cycle of the sub-cloud RH for the three setups (Figure 10d, j, and p) shows that longer periods of decoupling occur as the BL
 611 depth increases (elevated and prolonged mean sub-cloud RH corresponds to a poorly mixed BL). In both the *control* and *800-*
 612 *m* setups the BL is reasonably well mixed throughout the day. The presence of the aerosol layer enhances the midday coupling
 613 and weakens the cloud decay phase, producing a thicker cloud in the afternoon. However, for the *1000-m* setup the lowering
 614 of the cloud layer is not sufficient to overcome the decoupling that occurs, therefore there is no additional flux of moisture at
 615 midday and the cloud does not thicken, producing a positive SDE in the afternoon. As the BL deepens overnight, the dynamics
 616 become increasingly sensitive to the elevated absorbing aerosol layer (Figure 10c, i, and o). The result is a more pronounced
 617 decrease in the cloud growth phase overnight and a thinner cloud in the morning. The *800-m* and *1000-m* setups produce a
 618 strong positive SDE in the morning from day 2 onwards (Figure 10l and r), which dominates the daily mean SDE (Table 5).
 619 As described in Sect. 3.2.2, reductions in w_e and below-cloud moisture fluxes set up a feedback mechanism that decreases the
 620 BL dynamics. As the BL deepens this mechanism occurs more rapidly and may be further enhanced by reduced cloud-top
 621 longwave cooling that occurs when the LWP is sufficiently reduced. The reduction by $\sim 30 \text{ g m}^{-2}$ of the LWP in the *1000-m*
 622 setup is a large enough perturbation to reduce the longwave cloud-top cooling by $\sim 40\%$ and decrease buoyancy production.
 623



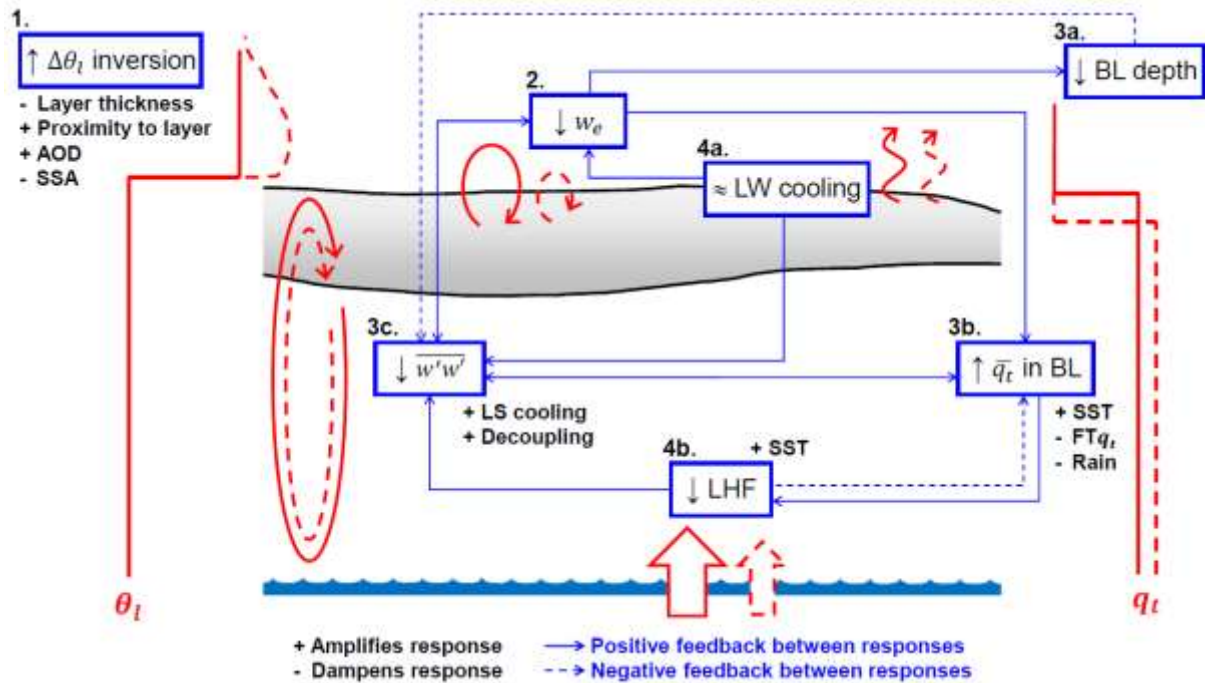
624

625 **Figure 10.** 3-day timeseries showing the initial response of the cloud to a 250 m thick layer of aerosol directly above the inversion
 626 with an aerosol optical depth of 0.2 from the a) – f) control setup with a boundary layer depth of 600 m, g) – l) 800-m setup, and m)
 627 – r) 1000-m setup. From top to bottom row, panels show the altitude of the cloud base and top, the liquid water path (LWP), the
 628 mean boundary layer (BL) vertical velocity variance ($w'w'$), the mean relative humidity (RH) between the ocean surface and the
 629 cloud base, changes to the BL water content as the mean total water content q_t and the total water path (TWP), and the semi-direct
 630 effect.

631 These results explain the different aerosol–layer sensitivities shown in Table 5. In all setups the enhanced temperature inversion
 632 weakens w_e and the mixing of warm, dry FT air into the cloud layer and enhances midday coupling. For the *control* setup there
 633 is little impact on BL dynamics, so the cloud becomes thicker due to enhanced sources of moisture; as the temperature inversion
 634 strengthens this response increases. As the BL deepens the BL dynamics are increasingly weakened, driving a reduction in
 635 sub-cloud sources of moisture and a thinner cloud; as the temperature inversion strengthens this response also increases. The

636 1000-m setup represents an extreme case of this scenario, whereas in the 800-m setup the enhanced coupling is sufficient to
 637 produce an increase in sub-cloud moisture flux during the afternoon, which acts to partially mitigate the cloud thinning.

638 **4 Discussion and conclusions**



639
 640 **Figure 11.** Summary of how the semi-direct effect manifests in a cross section of a stratocumulus-topped boundary layer. Solid red
 641 lines refer to the no-aerosol simulation and dashed red lines to the elevated absorbing aerosol-layer simulations. Key responses to
 642 the boundary layer profiles are depicted in the blue boxes and include the strength of the inversion layer ($\Delta\theta_I$ inversion), entrainment
 643 rate (w_e), boundary layer depth (BL depth), cloud-top longwave cooling (LW cooling), mean vertical motions in the boundary layer
 644 ($\overline{w'w'}$), mean total water content of the BL ($\overline{q_t}$), and the latent heat flux at the ocean surface (LHF). Solid (dashed) arrows between
 645 boxes represent positive (negative) feedbacks between responses. For each response we include properties of the aerosol layer,
 646 boundary layer, or model setup that amplify (denoted by +) or dampen (denoted by -) the response; this includes the aerosol layer
 647 thickness (Layer thickness), cloud-aerosol gap (Proximity to layer), the aerosol optical depth of the layer (AOD), the single scattering
 648 albedo of the aerosol layer (SSA), the sea surface temperature (SST), the water content of the free troposphere (FT q_t), precipitation
 649 (Rain), large-scale advective heat tendency (LS cooling), and the degree of boundary layer decoupling (Decoupling).

650
 651 Figure 11 summarises the findings of this study. The SDE manifests itself as a modification to the processes that maintain the
 652 supply of moisture to the cloud layer and are ultimately driven by the strengthened inversion layer and weakened entrainment
 653 rate caused by an absorbing aerosol layer above the inversion. The initial sequence of responses to an elevated layer of
 654 absorbing aerosol is summarised below, with numbers referring to each response labelled in Figure 11:

- 655 1. The absorbing aerosol layer produces a heat perturbation that results in a strengthened temperature inversion.

- 656 2. Buoyant parcels of air in the BL require more energy in order to push through the strengthened temperature inversion.
657 This weakens the entrainment rate (w_e) across the inversion layer.
- 658 3a. Weakened entrainment results in a decrease in the cloud top altitude and BL depth.
- 659 3b. The reduction in the entrainment of warm and dry air from the FT reduces the amount of mixing, reducing the sink
660 of q_t in the cloud layer and allowing the BL to maintain a greater RH. The result is an increase in \bar{q}_t , a small decrease
661 in BL temperature, and an increase in RH.
- 662 3c. Weakened entrainment reduces the production of buoyancy from evaporative cooling of entrained air, causing a
663 decrease in BL dynamics ($\overline{w'w'}$), especially overnight.
- 664 4a. Cloud-top longwave cooling remains largely unchanged due to the weak sensitivity to LWPs larger than 50 g m^{-2}
665 overnight and the relatively small changes in LWP during the daytime. The insulating effect of the aerosol layer only
666 weakly influences the net longwave fluxes and divergence above the cloud.
- 667 4b. Increased \bar{q}_t in the BL and weakened BL dynamics reduces the evaporation rate of water from the surface, as
668 evidenced by the reduction in latent heat flux (LHF).

669

670 According to the model sensitivity simulations presented, SDE is amplified through the following mechanisms:

- 671 – Geometrically thinner aerosol layers of high aerosol density and low SSA, which produce a stronger localised heat
672 perturbation.
- 673 – Aerosol layers close to the inversion, while larger cloud-aerosol gaps result in a delayed and weaker cloud response.
- 674 – Warmer SSTs, which enhance the flux of moisture to the BL. As a secondary response, the increased SST also drives
675 a stronger reduction in LHF and causes the BL to adjust at a quicker rate.

676 Conversely, SDE is reduced by:

- 677 – Precipitation that, as a sink of cloud liquid water, dampens the cloud response. It follows that any feedbacks that
678 result in an increase in precipitation further weakens the SDE.
- 679 – Increases to the large-scale advective heat tendency (stronger cooling), which are balanced by enhanced buoyancy
680 production from w_e and a more rapid BL adjustment.
- 681 – An increase in the moisture content of the FT, which increases the role that entrainment plays in the supply of moisture
682 to the BL.

683 Finally, an increase in the degree of decoupling in the BL increases the sensitivity of the BL dynamics to changes in w_e , driving
684 towards a positive daily mean SDE. Extreme cases result in a strong positive SDE from day two after applying the aerosol
685 perturbation.

686

687 Several feedbacks between responses occur as the BL adjusts to the perturbations. The key feedbacks occur in the sub-cloud
688 layer and can work together to greatly reduce the supply of moisture to the cloud layer. Processes that act to decrease $\overline{w'w'}$

689 also further decrease w_e and the LHF; these changes weaken the response of \bar{q}_t in the BL so that there is a weaker flux of q_v
690 to the cloud layer. Reduced w_e and a reduction in condensation at the base of the cloud layer weakens buoyancy production in
691 the cloud layer which acts to further decrease $\overline{w'w'}$ and w_e . These feedbacks are most pronounced during the cloud growth
692 phase overnight when the diurnal cycles of w_e , $\overline{w'w'}$, and LHF peak, resulting in a weakened cloud growth phase and a thinner
693 cloud overnight and into the morning when the aerosol layer is present, thus producing a positive SDE. Longwave cloud-top
694 cooling is only weakly sensitive to changes in LWP above 50 gm^{-2} and therefore we do not see changes in the buoyancy
695 production from this process unless the LWP is significantly impacted, which occurs when the BL is decoupled. In this case
696 the reduced LWP further weakens the buoyancy production in the cloud layer, and consequently w_e and BL dynamics.

697

698 A second adjustment feedback on the cloud maintenance occurs through the reduced depth of the BL which acts to promote
699 coupling of the cloud and sub-cloud layers. In this case the feedback mechanism outlined previously acts in reverse so that
700 $\overline{w'w'}$, LHF, and the supply of q_v to the cloud layer increase. This weaker feedback mechanism likely occurs throughout the
701 diurnal cycle but only becomes important at midday when BL dynamics and sub-cloud moisture fluxes are at their weakest
702 and most sensitive to small changes. This adjustment results in reduced cloud decay throughout the afternoon and a thicker
703 cloud, and thus negative SDE, when the elevated layer of absorbing aerosol is present. The strength of this feedback mechanism
704 decreases as the degree of BL decoupling increases until the mechanism ceases to have any impact on the BL; in our study
705 this occurs when the BL is 1000 m deep.

706

707 The sign and magnitude of the SDE from elevated layers of absorbing aerosol is sensitive to the layer properties and BL
708 properties, especially the diurnal variations in coupling between the cloud and sub-cloud layers. For coupled BLs, the SDE on
709 the first day after adding the absorbing aerosol layer is slightly positive unless the aerosol layer is close to the inversion layer.
710 On the second and third day the SDE is strongly negative and peaks on the second day. Generally, for coupled BLs the SDE
711 is of opposite sign to the DRE and often greater in magnitude, resulting in a small or negative total radiative effect for aerosol-
712 radiation interactions from elevated absorbing aerosol layers. For BLs that show characteristics of being decoupled for most
713 of the diurnal cycle the SDE is positive for all three days and increases in magnitude throughout; as the BL becomes more
714 decoupled the magnitude of the SDE increases. For decoupled BLs the SDE acts to enhance the DRE, resulting in a larger total
715 radiative effect.

716

717 The increased LWP and negative SDE in the well-mixed coupled BL experiments is consistent with satellite observations over
718 the southeast Atlantic from Adebisi and Zuidema (2018) and Wilcox (2012). However, our LEM simulations suggest a positive
719 SDE in decoupled BL regions, such as near the stratocumulus-to-cumulus transition region. In reality, the BL may not be as
720 decoupled as in the simulations. The deepening BL is usually accompanied by an increasing SST (Sandu and Stevens, 2011)
721 which was not represented in our simulations; the increase in SST would provide a considerably larger flux of moisture from

722 the surface and enhance the production of buoyancy at the surface which may act to weaken the sensitivity of the BL to changes
723 in dynamics. The aerosol-layer sensitivity experiments in section 3.3 suggest that the daily mean SDE strongly weakens as the
724 distance of the gap between the cloud top and aerosol layer increases. Table 3 shows that on the second day of the simulation
725 no gap results in a daily mean SDE of -7 Wm^{-2} compared to -0.4 Wm^{-2} for a 500 m gap. Additionally, even for a large
726 perturbation (AOD of 0.5) the daily mean SDE in the initial 24 hours of the 50 m gap experiment is only 1 Wm^{-2} . These results
727 are in general agreement with the stratocumulus-to-cumulus transition LES studies by Yamaguchi et al. (2015) and Zhou et
728 al. (2017) which suggest that only those elevated smoke layers that are very close, or in direct contact with, the cloud layer
729 impact the cloud properties. Combined with the satellite observations in Fig. 1 these results suggest the overall SDE from
730 elevated layers of aerosol over the Southeast Atlantic is weak. However, it is worth noting that Yamaguchi et al. (2015) and
731 Zhou et al. (2017) used the same case study (Sandu and Stevens, 2011) yet found opposing results on whether the absorbing
732 aerosol layer inhibits or hastens the transition to cumulus. Yamaguchi et al. (2015) state that throughout their simulations the
733 BL is decoupled below 800 m, whereas in Zhou et al. (2017) vertical mixing within the BL continues until the inversion height
734 exceeds $\sim 1.4 \text{ km}$ (Zhou et al., 2017; Fig. 1b). Our results highlight that the cloud response is sensitive to the diurnal variations
735 in BL mixing, which may explain these opposing results. Additionally, inconsistent responses between LES models can also
736 arise through differences in the representation of processes, including unresolved sub-grid scale turbulence (Stevens et al.,
737 2005) and microphysics (van der Dussen et al., 2013). Our results show that the heat perturbation above the cloud layer impacts
738 all aspects of the BL profile, therefore it would be beneficial to repeat this study using other LES models to test our conclusions.

739

740 Satellite products provide an excellent opportunity to observe aerosol–cloud and aerosol–radiation interactions in remote
741 locations such as the southeast Atlantic Ocean, however most instruments are on polar orbiting satellites that only provide
742 observations from a limited window within the diurnal cycle of the clouds. Our simulations suggest the cloud response to
743 elevated absorbing aerosol layers and the SDE display important diurnal variations so a single observation is unlikely to be
744 representative of the daily mean response. Important changes to the cloud properties occur overnight and play a considerable
745 role in the SDE of the morning period, yet little is known about the impact from absorbing aerosol layers overnight. Future
746 studies should use geostationary satellite observations to investigate the full diurnal cycle of the SDE.

747

748 For a well-mixed coupled BL, the initial cloud and radiative response depend on small-scale processes, such as entrainment
749 and turbulence, which must to be parameterised in climate models. Gordon et al. (2018) used a nested regional model within
750 the Hadley Centre Global Environment Model (HadGEM) to investigate the impact of an incoming elevated plume of smoke
751 in the southeast Atlantic. They found that the elevated aerosol layer reduced cloud top height and enhanced LWP through a
752 reduction in w_e driven by localised heating at or just above the cloud layer of $\sim 6 \text{ K}$. The importance of the weakened w_e aligns
753 well with the LES results of the present study, but the magnitude of the cloud and radiative response are much greater in
754 HadGEM, with an LWP increase of 90%, an increase in cloud fraction of 19% and a mean SDE of -30 Wm^{-2} . Gordon et al.
755 (2018) do not find a consistent longer-term (~ 3 days) reduction in LWP following BL adjustments. In the LES simulations

756 presented here, cloud fraction remained $\sim 100\%$, which may explain the smaller SDE than Gordon et al. (2018). Additionally,
757 concurrent aerosol-cloud interactions may modify the underlying cloud properties, which may act to amplify the SDE. The
758 lack of BL adjustment may be due to processes that are not explicitly treated in HadGEM, such as BL turbulence and
759 subsequent missing feedbacks on surface fluxes, or due to aerosol–cloud interactions not represented in the LES. Alternatively,
760 differences may be due to different simulated cases. The trajectory analysis of Gordon et al. (2018) suggests that their BL air
761 mass traverses the study region more quickly than the absorbing aerosol layer, which may prevent the BL adjustments from
762 occurring.

763

764 In our simulations the SST and subsidence rate are held constant for the whole duration whereas real stratocumulus decks tend
765 to experience an increasing SST and decreasing subsidence rate. An increasing SST increases surface latent heat fluxes, cloud
766 liquid water content, and the strength of BL eddies, and acts to deepen the BL through increased entrainment and enhance
767 decoupling of the sub–cloud layer (Bretherton and Wyant, 1997). As the cloud is advected over the warmer sea surface the
768 enhanced flux of moisture would act to increase the magnitude of the SDE and prevent the BL from drying out as quickly.
769 Simultaneously, the enhanced decoupling of the sub–cloud layer may result in BL dynamical feedbacks that result in a
770 reduction in LWP (see Figure 10). Our model uses a Eulerian framework where the absorbing aerosol layer remains at a
771 constant height above the cloud whereas the heat perturbation is allowed to subside into the cloud. In reality the aerosol layer
772 may also subside. The sensitivity experiments in Sect. 3.3 show that as the aerosol layer approaches the cloud layer the SDE
773 increases, therefore if we were to represent aerosol layer subsidence we would expect an enhanced cloud response and SDE.

774

775 Changes to the aerosol distribution within the cloud or in the cloud droplet distribution have not been considered in this study.
776 A weakened w_e increases condensate in the cloud and likely results in an increase in cloud droplet effective radius (r_e). This
777 would promote warm rain process and enhance precipitation, thus reducing the LWP and amplifying the reduction in BL
778 dynamics. These combined effects could lead to a decrease in LWP and shift the SDE towards a positive sign at a quicker rate
779 than suggested by the LES. For the cases where the aerosol layer is directly above the cloud layer an enhanced flux of CCN
780 into the BL would be expected and would act to reduce r_e , suppress precipitation, and act to enhance buoyancy production.
781 However, in-situ observations routinely find that the layers of smoke over the Southeast Atlantic are embedded in moist layers
782 (Adebisi et al., 2015), which could increase the flux of water from the free-troposphere and act to mitigate the changes that
783 occurs alongside an increased CCN. The introduction of the absorbing aerosol into the cloud layer would additionally enhance
784 cloud evaporation and act to thin the cloud layer (Hill and Dobbie, 2008; Johnson et al., 2004). Thus, although the experiments
785 where the aerosol layer is directly above the inversion result in the most strongly negative SDE, the response would be at least
786 partially mitigated if the aerosol distribution was represented explicitly, decreasing further the role that SDE plays in the total
787 radiative effect of elevated layers of absorbing aerosol. Extending the present study using a binned microphysics scheme would
788 include the additional response of the droplet size distribution and using an aerosol scheme would include the additional
789 impacts the weakened w_e has on the availability of CCN and subsequent cloud response.

790 **5 Appendix**

791 This appendix describes how the AOD and SSA is prescribed in elevated aerosol layer experiments, along with the geometric
 792 thickness of the aerosol layer and the distance between the inversion layer and the aerosol base. In each call to the radiation
 793 scheme the desired AOD and SSA are used to determine the mass mixing ratio of two aerosol species, water-soluble like (WS)
 794 and biomass-burning like (BB).

795

796 For a single wavelength, the AOD between the altitudes z_0 and z , corresponding to the base and top of the aerosol layer
 797 respectively, is calculated as:

$$\text{AOD} = \sum_{i=z_0}^z \sum_{j=WS, BB} (K_{scat_j} + K_{abs_j}) \cdot q_{i,j} \cdot \rho_i \cdot dz_i \quad (\text{A1})$$

798

799 where K_{scat} and K_{abs} are the specific scattering and absorption coefficients, respectively, for the aerosol species j , in units
 800 $\text{m}^2 \text{kg}^{-1}$, with mass mixing ratio q in $\text{kg kg}_{\text{dry}}^{-1}$, at each model level i of geometric thickness dz in m, and density of dry air ρ in
 801 kg m^{-3} . If the mass mixing ratio of each species is assumed equal and constant with height ($q_{WS} = q_{BB}$ and $q_i = q$), Eq. A1
 802 becomes:

803

$$q \cdot \sum_{i=z_0}^z \rho_i \cdot dz_i = \frac{\text{AOD}}{\sum_{j=WS, BB} K_{scat_j} + K_{abs_j}} \quad (\text{A2})$$

804

805 We incorporate a factor X_{SSA} into Eq. A2 that can be used to describe the relative ratio of WS mass to BB mass so that Eq. A2
 806 becomes:

$$q \cdot \sum_{i=z_0}^z \rho_i \cdot dz_i = \frac{\text{AOD}}{(K_{scat_{WS}} + K_{abs_{WS}}) + X_{SSA} \cdot (K_{scat_{BB}} + K_{abs_{BB}})} \quad (\text{A3})$$

807

808 Equation A3 can be re-arranged to give q for a given AOD:

809

$$q = \frac{\text{AOD}_{\text{constant}}}{\sum_{i=z_0}^z \rho_i \cdot dz_i} \quad (\text{A4})$$

810 where

$$\text{AOD}_{\text{constant}} = \frac{\text{AOD}}{(K_{scat_{WS}} + K_{abs_{WS}}) + X_{SSA} \cdot (K_{scat_{BB}} + K_{abs_{BB}})} \quad (\text{A5})$$

811

812 Therefore for the two aerosol species:

$$q_j = \begin{cases} q, & j = WS \\ X_{SSA} \cdot q, & j = BB \end{cases} \quad (\text{A6})$$

813

814 The overall SSA is calculated as:

815

$$SSA = \frac{K_{scat_{WS}} + X_{SSA} \cdot K_{scat_{BB}}}{K_{scat_{WS}} + X_{SSA} \cdot K_{scat_{BB}} + K_{abs_{WS}} + X_{SSA} \cdot K_{abs_{BB}}} \quad (\text{A7})$$

816

817 Equation A7 can be re-arranged to solve for X_{SSA}

818

$$X_{SSA} = \frac{K_{scat_{WS}} - SSA \cdot (K_{scat_{WS}} + K_{abs_{WS}})}{SSA \cdot (K_{scat_{BB}} + K_{abs_{BB}}) - K_{scat_{BB}}} \quad (\text{A8})$$

819

820 At the beginning of the simulation X_{SSA} and $AOD_{constant}$ are calculated using Equations A8 and A5, respectively, using the
 821 shortwave extinction coefficients of the aerosols for the wavelength band 320 – 690 nm and the prescribed AOD and SSA. At
 822 each horizontal grid point q is then calculated using Eq. A4 for the elevated aerosol layer where z_0 is the base of the aerosol
 823 layer, and z is the top of the aerosol layer. The mass mixing ratio of each species is calculated using Eq. A6 and finally the
 824 mass mixing ratio profiles of WS and BB applied to the radiation scheme.

825 **6 Author contribution**

826 RJH, NB, EJH, and AAH designed the methodology and experiments. AAH provided model expertise and assistance. RJH
 827 setup, performed, and post-processed the simulations. RJH, NB, EJH, and AAH analysed the results. RJH provided all
 828 visualisations and wrote the initial manuscript draft. NB, EJH, and AAH provided revisions and commentary on the
 829 manuscript.

830 **7 Competing interests**

831 The authors declare that they have no conflict of interest.

832 **8 Acknowledgments**

833 This research was funded by the UK Natural Environment Research Council (NERC) CLOUDS and Aerosol Radiative Impacts
 834 and Forcing: Year 2016 (CLARIFY-2016) project NE/L013479/1. We acknowledge use of the Monsoon system, a
 835 collaborative facility supplied under the Joint Weather and Climate Research Programme, a strategic partnership between the

836 Met Office and the Natural Environment Research Council. The CALIOP data were obtained from the NASA Langley
837 Research Center Atmospheric Science Data Center.

838 **9 References**

839 Abel, S. J., Walters, D. N. and Allen, G.: Evaluation of stratocumulus cloud prediction in the Met Office
840 forecast model during VOCALS-REx, *Atmos. Chem. Phys.*, 10(21), 10541–10559, doi:10.5194/acp-10-
841 10541-2010, 2010.

842 Ackerman, A. S., vanZanten, M. C., Stevens, B., Savic-Jovicic, V., Bretherton, C. S., Chlond, A., Golaz,
843 J.-C., Jiang, H., Khairoutdinov, M., Krueger, S. K., Lewellen, D. C., Lock, A., Moeng, C.-H., Nakamura,
844 K., Petters, M. D., Snider, J. R., Weinbrecht, S. and Zulauf, M.: Large-Eddy Simulations of a Drizzling,
845 Stratocumulus-Topped Marine Boundary Layer, *Mon. Weather Rev.*, 137(3), 1083–1110,
846 doi:10.1175/2008MWR2582.1, 2009.

847 Adebisi, A. A. and Zuidema, P.: Low cloud cover sensitivity to biomass-burning aerosols and meteorology
848 over the Southeast Atlantic, *J. Clim.*, 31(11), 4329–4346, doi:10.1175/JCLI-D-17-0406.1, 2018.

849 Adebisi, A. A., Zuidema, P. and Abel, S. J.: The convolution of dynamics and moisture with the presence
850 of shortwave absorbing aerosols over the southeast Atlantic, *J. Clim.*, 28(5), 1997–2024,
851 doi:10.1175/JCLI-D-14-00352.1, 2015.

852 Albrecht, B. A., Jensen, M. P. and Syrett, W. J.: Marine boundary layer structure and fractional
853 cloudiness, *J. Geophys. Res.*, 100222(20), 209–14, doi:10.1029/95JD00827, 1995.

854 Bond, T. C., Doherty, S. J., Fahey, D. W., Forster, P. M., Berntsen, T., DeAngelo, B. J., Flanner, M. G.,
855 Ghan, S., Kärcher, B., Koch, D., Kinne, S., Kondo, Y., Quinn, P. K., Sarofim, M. C., Schultz, M. G.,
856 Schulz, M., Venkataraman, C., Zhang, H., Zhang, S., Bellouin, N., Guttikunda, S. K., Hopke, P. K.,
857 Jacobson, M. Z., Kaiser, J. W., Klimont, Z., Lohmann, U., Schwarz, J. P., Shindell, D., Storelvmo, T.,
858 Warren, S. G. and Zender, C. S.: Bounding the role of black carbon in the climate system: A scientific
859 assessment, *J. Geophys. Res. Atmos.*, 118(11), 5380–5552, doi:10.1002/jgrd.50171, 2013.

860 Bony, S. and Dufresne, J. L.: Marine boundary layer clouds at the heart of tropical cloud feedback
861 uncertainties in climate models, *Geophys. Res. Lett.*, 32(20), 1–4, doi:10.1029/2005GL023851, 2005.

862 Boucher, O., Randall, D., Artaxo, P., Bretherton, C., Feingold, G., Forster, P., Kerminen, V.-M., Kondo,
863 Y., Liao, H., Lohmann, U., Rasch, P., Satheesh, S. K., Sherwood, S., Stevens, B. and Zhang, X.-Y.:
864 IPCC AR5 Clouds and Aerosols, in *Climate Change 2013 - The Physical Science Basis*, pp. 571–658,
865 Cambridge University Press, Cambridge, United Kingdom and New York, NY, USA., 2013.

866 Bretherton, C. S. and Wyant, M. C.: Moisture Transport, Lower-Tropospheric Stability, and Decoupling
867 of Cloud-Topped Boundary Layers, *J. Atmos. Sci.*, 54(1), 148–167, doi:10.1175/1520-
868 0469(1997)054<0148:MTL TSA>2.0.CO;2, 1997.

869 Bretherton, C. S., Blossey, P. N. and Jones, C. R.: Mechanisms of marine low cloud sensitivity to
870 idealized climate perturbations: A single-LES exploration extending the CGILS cases, *J. Adv. Model.*
871 *Earth Syst.*, 5(2), 316–337, doi:10.1002/jame.20019, 2013.

872 Chand, D., Wood, R., Anderson, T. L., Satheesh, S. K. and Charlson, R. J.: Satellite-derived direct
873 radiative effect of aerosols dependent on cloud cover, *Nat. Geosci.*, 2(3), 181–184,
874 doi:10.1038/ngeo437, 2009.

875 Cook, J. and Highwood, E. J.: Climate response to tropospheric absorbing aerosols in an intermediate
876 general-circulation model, *Q. J. R. Meteorol. Soc.*, 130(596), 175–191, doi:10.1256/qj.03.64, 2004.

877 Costantino, L. and Bréon, F. M.: Aerosol indirect effect on warm clouds over South-East Atlantic, from
878 co-located MODIS and CALIPSO observations, *Atmos. Chem. Phys.*, 13(1), 69–88, doi:10.5194/acp-13-
879 69-2013, 2013.

880 Das, S., Harshvardhan, H., Bian, H., Chin, M., Curci, G., Protonotariou, A. P., Mielonen, T., Zhang, K.,
881 Wang, H. and Liu, X.: Biomass burning aerosol transport and vertical distribution over the South African-
882 Atlantic region, *J. Geophys. Res.*, 122(12), 6391–6415, doi:10.1002/2016JD026421, 2017.

883 van der Dussen, J. J., de Roode, S. R., Ackerman, A. S., Blossey, P. N., Bretherton, C. S., Kurowski, M.
884 J., Lock, A. P., Neggers, R. A. J., Sandu, I. and Siebesma, A. P.: The GASS/EUCLIPSE model
885 intercomparison of the stratocumulus transition as observed during ASTEX: LES results, *J. Adv. Model.*
886 *Earth Syst.*, 5(3), 483–499, doi:10.1002/jame.20033, 2013.

887 Edwards, J. M. and Slingo, A.: Studies with a flexible new radiation code. I: Choosing a configuration for
888 a large-scale model, *Q. J. R. Meteorol. Soc.*, 122(531), 689–719, doi:10.1256/smsqj.53106, 1996.

889 Efstathiou, G. A. and Beare, R. J.: Quantifying and improving sub-grid diffusion in the boundary-layer
890 grey zone, *Q. J. R. Meteorol. Soc.*, 141(693), 3006–3017, doi:10.1002/qj.2585, 2015.

891 Efstathiou, G. A., Beare, R. J., Osborne, S. and Lock, A. P.: Grey zone simulations of the morning
892 convective boundary layer development, *J. Geophys. Res. Atmos.*, 121(9), 4769–4782,
893 doi:10.1002/2016JD024860, 2016.

894 Feingold, G., Koren, I., Wang, H., Xue, H. and Brewer, W. A.: Precipitation-generated oscillations in open
895 cellular cloud fields, *Nature*, 466(7308), 849–852, doi:10.1038/nature09314, 2010.

896 Garrett, T. J. and Zhao, C.: Increased Arctic cloud longwave emissivity associated with pollution from
897 mid-latitudes, *Nature*, 440(7085), 787–789, doi:10.1038/nature04636, 2006.

898 Gordon, H., Field, P. R., Abel, S. J., Dalvi, M., Grosvenor, D. P., Hill, A. A., Johnson, B. T., Miltenberger,
899 A. K., Yoshioka, M. and Carslaw, K. S.: Large simulated radiative effects of smoke in the south-east
900 Atlantic, *Atmos. Chem. Phys.*, 18(20), 15261–15289, doi:10.5194/acp-18-15261-2018, 2018.

901 Gray, M. E. B., Brown, A. R., Lock, A. P. and Petch, J.: Version 2.3 Of The Met Office Large Eddy Model:
902 Part III. Software Documentation, Met Office, Bracknell, UK., 2001.

903 Hartmann, D. L. and Short, D. A.: On the Use of Earth Radiation Budget Statistics for Studies of Clouds
904 and Climate, *J. Atmos. Sci.*, 37(6), 1233–1250, doi:10.1175/1520-
905 0469(1980)037<1233:OTUOER>2.0.CO;2, 1980.

906 Hartmann, D. L., Ockert-Bell, M. E. and Michelsen, M. L.: Hartmann_EtAl_1992_EnergyBalance, *J.*
907 *Clim.*, 5(November), 1281–1304, doi:Doi 10.1175/1520-0442(1992)005<1281:Teocto>2.0.Co;2, 1992.

908 Hignett, P.: Observations of Diurnal Variation in a Cloud-capped Marine Boundary Layer, *J. Atmos. Sci.*,

- 909 48(12), 1474–1482, doi:10.1175/1520-0469(1991)048<1474:OODVIA>2.0.CO;2, 1991.
- 910 Hill, A. A. and Dobbie, S.: The impact of aerosols on non-precipitating marine stratocumulus. II: The
911 semi-direct effect, *Q. J. R. Meteorol. Soc.*, 134(634 A), 1155–1165, doi:10.1002/qj.277, 2008.
- 912 Hill, A. A., Dobbie, S. and Yin, Y.: The impact of aerosols on non-precipitating marine stratocumulus. I:
913 Model description and prediction of the indirect effect, *Q. J. R. Meteorol. Soc.*, 134(634 A), 1143–1154,
914 doi:10.1002/qj.278, 2008.
- 915 Hill, A. A., Feingold, G. and Jiang, H.: The Influence of Entrainment and Mixing Assumption on Aerosol–
916 Cloud Interactions in Marine Stratocumulus, *J. Atmos. Sci.*, 66(5), 1450–1464,
917 doi:10.1175/2008JAS2909.1, 2009.
- 918 Hill, A. A., Field, P. R., Furtado, K., Korolev, A. and Shipway, B. J.: Mixed-phase clouds in a turbulent
919 environment. Part 1: Large-eddy simulation experiments, *Q. J. R. Meteorol. Soc.*, 140(680), 855–869,
920 doi:10.1002/qj.2177, 2014.
- 921 Johnson, B. T., Shine, K. P. and Forster, P. M.: The semi-direct aerosol effect: Impact of absorbing
922 aerosols on marine stratocumulus, *Q. J. R. Meteorol. Soc.*, 130(599 PART B), 1407–1422,
923 doi:10.1256/qj.03.61, 2004.
- 924 Kato, S., Sun-Mack, S., Miller, W. F., Rose, F. G., Chen, Y., Minnis, P. and Wielicki, B. A.: Relationships
925 among cloud occurrence frequency, overlap, and effective thickness derived from CALIPSO and
926 CloudSat merged cloud vertical profiles, *J. Geophys. Res.*, 115, D00H28, doi:10.1029/2009JD012277,
927 2010.
- 928 Kato, S., Rose, F. G., Sun-Mack, S., Miller, W. F., Chen, Y., Rutan, D. A., Stephens, G. L., Loeb, N. G.,
929 Minnis, P., Wielicki, B. A., Winker, D. M., Charlock, T. P., Stackhouse, P. W., Xu, K.-M. and Collins, W.
930 D.: Improvements of top-of-atmosphere and surface irradiance computations with CALIPSO-, CloudSat-
931 , and MODIS-derived cloud and aerosol properties, *J. Geophys. Res.*, 116(D19), D19209,
932 doi:10.1029/2011JD016050, 2011.
- 933 Klein, S. A., Hall, A., Norris, J. R. and Pincus, R.: Low-Cloud Feedbacks from Cloud-Controlling Factors:
934 A Review, *Surv. Geophys.*, 38(6), 1307–1329, doi:10.1007/s10712-017-9433-3, 2017.
- 935 Koch, D. and Del Genio, A. D.: Black carbon semi-direct effects on cloud cover: review and synthesis,
936 *Atmos. Chem. Phys.*, 10(16), 7685–7696, doi:10.5194/acp-10-7685-2010, 2010.
- 937 Lee, I. Y.: Evaluation of cloud microphysics parameterizations for mesoscale simulations, *Atmos. Res.*,
938 24(1–4), 209–220, doi:https://doi.org/10.1016/0169-8095(89)90046-X, 1989.
- 939 Leon, D. C., Wang, Z. and Liu, D.: Climatology of drizzle in marine boundary layer clouds based on 1
940 year of data from CloudSat and Cloud-Aerosol Lidar and Infrared Pathfinder Satellite Observations
941 (CALIPSO), *J. Geophys. Res. Atmos.*, 114(8), D00A14, doi:10.1029/2008JD009835, 2009.
- 942 Lu, Z., Liu, X., Zhang, Z., Zhao, C., Meyer, K., Rajapakshe, C., Wu, C., Yang, Z. and Penner, J. E.:
943 Biomass smoke from southern Africa can significantly enhance the brightness of stratocumulus over the
944 southeastern Atlantic Ocean, *Proc. Natl. Acad. Sci.*, 115(12), 2924–2929,
945 doi:10.1073/pnas.1713703115, 2018.
- 946 Monin, A. S. and Obukhov, A. M.: Basic laws of turbulent mixing in the surface layer of the atmosphere,

947 Geophys. Dir. AF Cambridge Res. Cent., 24(151), 163–187, doi:10.1016/j.jallcom.2004.05.088, 1954.

948 Muhlbauer, A., McCoy, I. L. and Wood, R.: Climatology of stratocumulus cloud morphologies:
 949 Microphysical properties and radiative effects, *Atmos. Chem. Phys.*, 14(13), 6695–6716,
 950 doi:10.5194/acp-14-6695-2014, 2014.

951 Ovchinnikov, M., Ackerman, A. S., Avramov, A., Cheng, A., Fan, J., Fridlind, A. M., Ghan, S., Harrington,
 952 J., Hoose, C., Korolev, A., McFarquhar, G. M., Morrison, H., Paukert, M., Savre, J., Shipway, B. J.,
 953 Shupe, M. D., Solomon, A. and Sulia, K.: Intercomparison of large-eddy simulations of Arctic mixed-
 954 phase clouds: Importance of ice size distribution assumptions, *J. Adv. Model. Earth Syst.*, 6(1), 223–
 955 248, doi:10.1002/2013MS000282, 2014.

956 Painemal, D., Kato, S. and Minnis, P.: Boundary layer regulation in the southeast Atlantic cloud
 957 microphysics during the biomass burning season as seen by the A-train satellite constellation, *J.*
 958 *Geophys. Res.*, 119(19), 11,288–11,302, doi:10.1002/2014JD022182, 2014.

959 Peers, F., Bellouin, N., Waquet, F., Ducos, F., Goloub, P., Mollard, J., Myhre, G., Skeie, R. B., Takemura,
 960 T., Tanré, D., Thieuleux, F. and Zhang, K.: Comparison of aerosol optical properties above clouds
 961 between POLDER and AeroCom models over the South East Atlantic Ocean during the fire season,
 962 *Geophys. Res. Lett.*, 43(8), 3991–4000, doi:10.1002/2016GL068222, 2016.

963 Penner, J. E., Zhang, S. Y. and Chuang, C. C.: Soot and smoke aerosol may not warm climate, *J.*
 964 *Geophys. Res. Atmos.*, 108(D21), doi:10.1029/2003JD003409, 2003.

965 Rajapakshe, C., Zhang, Z., Yorks, J. E., Yu, H., Tan, Q., Meyer, K., Platnick, S. and Winker, D. M.:
 966 Seasonally transported aerosol layers over southeast Atlantic are closer to underlying clouds than
 967 previously reported, *Geophys. Res. Lett.*, 44(11), 5818–5825, doi:10.1002/2017GL073559, 2017.

968 de Roode, S. R., Sandu, I., van der Dussen, J. J., Ackerman, A. S., Blossey, P., Jarecka, D., Lock, A.,
 969 Siebesma, A. P. and Stevens, B.: Large-Eddy Simulations of EUCLIPSE–GASS Lagrangian
 970 Stratocumulus-to-Cumulus Transitions: Mean State, Turbulence, and Decoupling, *J. Atmos. Sci.*, 73(6),
 971 2485–2508, doi:10.1175/JAS-D-15-0215.1, 2016.

972 De Roode, S. R., Siebesma, A. P., Gesso, S. D., Jonker, H. J. J., Schalkwijk, J. and Sival, J.: A mixed-
 973 layer model study of the stratocumulus response to changes in large-scale conditions, *J. Adv. Model.*
 974 *Earth Syst.*, 6(4), 1256–1270, doi:10.1002/2014MS000347, 2014.

975 Sakaeda, N., Wood, R. and Rasch, P. J.: Direct and semidirect aerosol effects of southern African
 976 biomass burning aerosol, *J. Geophys. Res.*, 116(D12), D12205, doi:10.1029/2010JD015540, 2011.

977 Sandu, I. and Stevens, B.: On the Factors Modulating the Stratocumulus to Cumulus Transitions, *J.*
 978 *Atmos. Sci.*, 68(9), 1865–1881, doi:10.1175/2011JAS3614.1, 2011.

979 Sandu, I., Stevens, B. and Pincus, R.: On the transitions in marine boundary layer cloudiness, *Atmos.*
 980 *Chem. Phys.*, 10(5), 2377–2391, doi:10.5194/acp-10-2377-2010, 2010.

981 Sherwood, S. C., Bony, S., Boucher, O., Bretherton, C., Forster, P. M., Gregory, J. M., Stevens, B.,
 982 Sherwood, S. C., Bony, S., Boucher, O., Bretherton, C., Forster, P. M., Gregory, J. M. and Stevens, B.:
 983 Adjustments in the Forcing-Feedback Framework for Understanding Climate Change, *Bull. Am.*
 984 *Meteorol. Soc.*, 96(2), 217–228, doi:10.1175/BAMS-D-13-00167.1, 2015.

985 Stevens, B., Moeng, C.-H., Ackerman, A. S., Bretherton, C. S., Chlond, A., de Roode, S., Edwards, J.,
986 Golaz, J.-C., Jiang, H., Khairoutdinov, M., Kirkpatrick, M. P., Lewellen, D. C., Lock, A., Müller, F.,
987 Stevens, D. E., Whelan, E. and Zhu, P.: Evaluation of Large-Eddy Simulations via Observations of
988 Nocturnal Marine Stratocumulus, *Mon. Weather Rev.*, 133(6), 1443–1462, doi:10.1175/MWR2930.1,
989 2005.

990 Stjern, C. W., Samset, B. H., Myhre, G., Forster, P. M., Hodnebrog, Ø., Andrews, T., Boucher, O.,
991 Faluvegi, G., Iversen, T., Kasoar, M., Kharin, V., Kirkevåg, A., Lamarque, J. F., Olivié, D., Richardson,
992 T., Shawki, D., Shindell, D., Smith, C. J., Takemura, T. and Voulgarakis, A.: Rapid Adjustments Cause
993 Weak Surface Temperature Response to Increased Black Carbon Concentrations, *J. Geophys. Res.*
994 *Atmos.*, 122(21), 11,462–11,481, doi:10.1002/2017JD027326, 2017.

995 Wilcox, E. M.: Stratocumulus cloud thickening beneath layers of absorbing smoke aerosol, *Atmos.*
996 *Chem. Phys.*, 10(23), 11769–11777, doi:10.5194/acp-10-11769-2010, 2010.

997 Wilcox, E. M.: Direct and semi-direct radiative forcing of smoke aerosols over clouds, *Atmos. Chem.*
998 *Phys.*, 12(1), 139–149, doi:10.5194/acp-12-139-2012, 2012.

999 Wood, R.: Stratocumulus Clouds, *Mon. Weather Rev.*, 140(8), 2373–2423, doi:10.1175/MWR-D-11-
1000 00121.1, 2012.

1001 Wyant, M. C., Wood, R., Bretherton, C. S., Mechoso, C. R., Bacmeister, J., Balmaseda, M. A., Barrett,
1002 B., Codron, F., Earnshaw, P., Fast, J., Hannay, C., Kaiser, J. W., Kitagawa, H., Klein, S. A., Köhler, M.,
1003 Manganello, J., Pan, H. L., Sun, F., Wang, S. and Wang, Y.: The PreVOCA experiment: Modeling the
1004 lower troposphere in the Southeast Pacific, *Atmos. Chem. Phys.*, 10(10), 4757–4774, doi:10.5194/acp-
1005 10-4757-2010, 2010.

1006 Yamaguchi, T., Feingold, G., Kazil, J. and McComiskey, A.: Stratocumulus to cumulus transition in the
1007 presence of elevated smoke layers, *Geophys. Res. Lett.*, 42(23), 10478–10485,
1008 doi:10.1002/2015GL066544, 2015.

1009 Zhang, Y., Stevens, B., Medeiros, B. and Ghil, M.: Low-cloud fraction, lower-tropospheric stability, and
1010 large-scale divergence, *J. Clim.*, 22(18), 4827–4844, doi:10.1175/2009JCLI2891.1, 2009.

1011 Zhou, X., Ackerman, A. S., Fridlind, A. M., Wood, R. and Kollias, P.: Impacts of solar-absorbing aerosol
1012 layers on the transition of stratocumulus to trade cumulus clouds, *Atmos. Chem. Phys.*, 17(20), 12725–
1013 12742, doi:10.5194/acp-17-12725-2017, 2017.

1014